Materials Advances

ROYAL SOCIETY OF CHEMISTRY

PAPER

View Article Online
View Journal | View Issue

Cite this: *Mater. Adv.*, 2025, 6, 9779

Enhanced synergistic photocatalysis: a thorough investigation of $Bi_2Sn_2O_7/C_3N_5$ heterojunctions

Adarsh Kumar,[ab] Deepak Tyagi,[ab] Sagnik Mitra,[ab] Jitendra Bahadur,[bc] Avesh K. Tyagi[b] and Kaustava Bhattacharyya*[ab]

The close bandgap alignment between graphitic-C_3N_5 (g-CN) and $Bi_2Sn_2O_7$ (BSN) facilitates effective heterojunction formation, enhancing charge separation and transport. This study explores the photocatalytic degradation of *ortho*-dichlorobenzene (*o*-DCB) using a series of $Bi_2Sn_2O_7$–g-C_3N_5 (BSN–CN) heterojunctions, which were synthesized hydrothermally with various dispersions of $Bi_2Sn_2O_7$ (BSN) on graphitic-C_3N_5 (g-CN). A thorough characterization was carried out using different techniques, including X-ray diffraction (XRD), diffuse reflectance spectroscopy (DRS-UV-Vis), X-ray photoelectron spectroscopy (XPS), high-resolution transmission electron microscopy (HR-TEM), field emission scanning electron microscopy (FE-SEM), photoluminescence (PL), time-resolved photoluminescence (TRPL), and cyclic voltammetry (CV). These analyses not only confirmed the formation of the heterojunctions but also revealed the effect of structural parameters that significantly influenced their photocatalytic behavior. These structural parameters mainly affected the kinetics, lifetime, and migration pathways of photogenerated electron–hole (e^-/h^+) pairs. The photocatalytic activity of these heterojunctions was tested for *o*-DCB degradation, representing dioxin and furan analogues, under visible light and ambient, liquid-phase conditions. The BSN–CN composites demonstrated superior photocatalytic performance compared to the individual components and their physical mixtures. Notably, the BSN–CN-15 (with 15% BSN dispersed over CN) sample, which had the highest BSN content, achieved almost complete mineralization of *o*-DCB at one of the fastest rates reported to date. A detailed structure–activity relationship was established, highlighting the roles of bandgap energy, valence band position, and surface charge in governing photocatalytic efficiency. Post-reaction XPS analysis further revealed changes in surface chemistry, shedding light on the degradation mechanism. Additionally, the formation of surface intermediates was investigated to better understand the photocatalytic pathway and guide future improvements in catalyst design.

Received 25th August 2025,
Accepted 24th October 2025

DOI: 10.1039/d5ma00954e

rsc.li/materials-advances

1. Introduction

Road maps for enhancing photocatalytic activity include substitutional elemental doping,[1–3] morphological manipulation,[4,5] and the deposition of noble metals as co-catalysts.[6] The limitations of photocatalysts with single-component structures could be overcome through a feasible strategy of constructing semiconductor heterojunctions.[7] $Bi_2Sn_2O_7$ (BSN), with a pyrochlore-related structure, has three distinct BSN polymorphs: α-monoclinic, β-face-centred cubic, and γ-cubic. The γ-cubic phase, embodying the pyrochlore structure, possesses a considerably dispersed valence band characterized by hybridized Bi $6s^26p^0$ and Sn $5s^05p^0$ states, along with a minor contribution from O-2p. This configuration gives rise to a deeply situated valence band state, which in turn facilitates the mobility of charge carriers. This, coupled with a narrow band gap, generally translates to the efficient utilization of electron–hole pairs, rendering γ-cubic BSN a potential photocatalyst in the visible light spectrum.[8] The dispersed nature of the s and p-orbitals, owing to the low effective masses for electrons and holes (e^-/h^+), further enhances the photocatalytic efficiency by enabling their facile transport to the surface.[9]

Among graphenic semiconductors, graphitic carbon nitride (g-C_3N_4), composed of tris-*s*-triazine (*s*-heptazine, C_6N_7) units bridged by nitrogen atoms to give a 2D graphitic structure, has attracted significant interest due to its outstanding electronic, optical and physicochemical properties.[10] Recently, a new type of N-rich carbon nitride (C_3N_5) possessing wider light absorption ability (>600 nm) has been synthesized by different groups with various precursors.[11–14] The stoichiometrically rich nitrogen content can be tuned using N-rich precursors, and the resulting N-rich CNs (*e.g.* C_3N_5 having $E_g \sim 2$ eV) exhibit enhanced visible light absorption, and local electron concentration at the edge

[a] *Chemistry Division, Bhabha Atomic Research Centre, Mumbai-40085, India. E-mail: kaustava@barc.gov.in*
[b] *Homi Bhabha National Institute, Mumbai-400 094, India*
[c] *Solid State Physics Division, Bhabha Atomic Research Centre, Mumbai-400 085, India*

N atoms near the crystal defects acts as catalytically active sites necessary for CO_2 conversion.[15] The material demonstrates a low Gibbs free energy for CO_2 reduction compared with H_2 production, indicating that CO_2 reduction is more favourable than H_2 evolution.[16] Moreover, the ring size and pore size of C_3N_5 are larger than those of g-C_3N_4 due to the presence of multiple π-bonded N atoms within the C_3N_5 structure. These unique properties facilitate the efficient adsorption of the –COOH intermediate and subsequent CH_4 evolution as a final product in photocatalytic CO_2 reduction.[16] However, there have been limited reports on photocatalytic CO_2 reduction using N-rich CNs due to the fast kinetics of electron–hole recombination and low conductivity.[15]

1,2-Dichlorobenzene (*o*-DCB), has been chosen frequently as a model compound for polychlorinated dibenzo- dioxins/polychlorinated dibenzo-furans (PCDDs/PCDFs) which minimises the dangers, complexities and cost of PCDDs/PCDFs.[17,18] Thus, the development for mitigation of *o*-DCB is urgent. Up till date, catalytic oxidation or combustion has been the main removal method for PCDD and PCDFs, and has been extensively studied by some research groups. The mitigation of *o*-DCB in the liquid phase is as important as in the gas phase, as most of the dioxin and furan enter the food cycle from the water and lipid phase.

Recently, there have been a lot of studies on different heterojunctions including g-carbon nitrides. Jiang *et al.* have reported a high-performance g-C_3N_5/Bi_2SiO_5 heterojunction photocatalyst where enhanced activity was reported due to the formation of an S-scheme heterojunction and the introduction of specific electron pathways.[6] Guo *et al.* have described a highly efficient $Bi_2Sn_2O_7$/C_3N_4 composite for the degradation of dyes like rhodamine B, showcasing an effective technique for the charge separation of generated holes and electrons.[19] Li *et al.* performed photocatalytic degradation of norfloxacin using a similar system, reporting improvement in the separation efficiency of photogenerated electron holes, which induces enhanced photocatalytic performance. Two-dimensional (2D) heterojunctions with unique electronic features are present at the nanoscale interfacial region, which clearly results in the strong possibility of efficient carrier transport and migration. Wang *et al.* reported a multi-heterojunction material, $Bi_4O_5I_2$/g-C_3N_5/$Bi_2O_2CO_3$, for the degradation of tetracycline hydrochloride and acid red B, where the ternary heterojunction material designed through the matching energy band structure exhibits excellent redox ability, and the radical capture and photoelectric tests prove the rationality of the design system.[20] AgI/C_3N_5 catalysts achieved 10.1 times the disinfection efficiency of C_3N_5, and 5.6 times that of AgI, with a 1 min reaction time, owing to their type-II heterojunction.[21] The S-scheme Ag/Ag_2CO_3/C_3N_5 heterojunction photocatalyst exhibits markedly enhanced photocatalytic activity toward oxytetracycline degradation facilitated by its efficient separation of powerful charge carriers.[22] Similarly, the $Mn_{0.5}Cd_{0.5}S$/C_3N_5 S-scheme heterojunction exhibits extraordinary catalytic performance, achieving a higher tetracycline abatement rate than $Mn_{0.5}Cd_{0.5}S$ or C_3N_5 alone, primarily because of the synergistic effect of efficient spatial photo-carrier separation.[23] Similarly, S-scheme heterojunction photocatalysts of $Mn_{0.5}Cd_{0.5}S$/BiOBr were used in removing pharmaceuticals and chromium contamination with oxygen vacancies improving the photocatalytic efficiency manifold.[24]

$Bi_2Sn_2O_7$ (BSN) is a well-explored photocatalyst with a low-lying valence band oxidation potential, utilized for many oxidation reactions, and equivalently, the reduction potential is negative enough to be utilized in several photoreduction pathways. However, while the formation of certain heterojunctions of BSN, mainly with g-C_3N_4 and graphene, has been explored previously, a lot of other heterojunctions, consisting of A_2BO_5 or ABO_3, have also been studied, mainly with g-C_3N_4 or g-C_3N_5. Several other works have investigated the formation of a heterojunction with other pyrochlores ($A_2B_2O_7$), including $Ce_2Zr_2O_7$;[25] defect pyrochlores like $Bi_{1.8}Fe_{0.2}WO_6$ with g-C_3N_5;[26] and ferro-electric pyrochlores of $Bi_{1.65}Fe_{1.16}Nb_{1.12}O_7$ with g-C_3N_4 for their improved photocatalytic efficiency.[27] However, there are very limited reports in the literature on the $Bi_2Sn_2O_7$–g-C_3N_5 heterostructure, and this is the first effort towards its investigation. Our group has recently shown the effect of asymmetry, and how the highly asymmetric BSN pyrochlore with the maximum coordination number of Bi of 5 leads to a strong increase in the photocatalytic properties owing to its structure.[28] The g-C_3N_5 possesses a similar Fermi edge to that of BSN, making it a strong candidate for the formation of a heterojunction with BSN.

In the present study, a facile strategy was developed for the synthesis of a $Bi_2Sn_2O_7$/g-C_3N_5 heterojunction to overcome the challenges associated with the dispersion of these nanomaterials over g-C_3N_5 under hydrothermal conditions, owing to the typical structure of BSN. The major focus is on the utilization of heterojunctions for the photocatalytic degradation of *o*-DCB. Although the literature contains many studies of the photodegradation of *o*-DCB in the gas phase, there are very few works to date on the direct degradation of an *o*-DCB–water mixture. This work involves the direct mineralization of *o*-DCB at the liquid–solid interface. *o*-DCB degradation is one of the most kinetically demanding reactions, requiring a low-lying valence band with sufficient oxidation potential. In order to overcome this challenge, the present study represents the first attempt to achieve direct mineralization of *o*-DCB within a defined time frame. The different photocatalytic parameters regulating the heterojunction photocatalytic properties are studied in detail. The study also explores various intermediates involved in the mineralization of *o*-DCB, aiming to elucidate the mechanism underlying the mineralization of *o*-DCB facilitated by these heterojunctions. The effects of band gap, surface charge, valence band potential and electronic density of these heterojunction systems that control their photocatalytic properties and thereby the surface properties leading to different intermediates formed in the mineralization of *o*-DCB are elucidated. The BSN–CN set of catalysts effectively degrades *o*-DCB, and these are among the best-performing catalysts reported so far (as shown in Table 1), primarily owing to the effect of the heterojunction. The detailed characterization, including band alignment and charge transfer mechanisms, provides a fundamental understanding of how this combination enhances photocatalytic activity.

Table 1 A comparative evaluation of advanced catalytic systems for *o*-DCB. D = 500 W Xe-lamp + UV cut off filter (>400 nm), visible light; HT = hydrothermal; ST = solvothermal; C = calcination; US = ultrasound

S. no.	Catalyst formulation (under visible light)	Synthetic methodology	Amount of *o*-DCB and catalyst	Irradiation source used	Catalytic performance (with time)	Ref.
1	$AgInS_2/TiO_2$ heterostructure	HT + modifications	5 μL liquid & 0.03 g catalyst (gas–solid interface)	Visible source (D)	50.4% (~8 h)	29
2	$BiPO_4/BiOBr$ p–n heterojunction	ST	5 μL liquid & 0.02 g catalyst (gas–solid interface)	Visible source (D)	53.6% (~8 h)	30
3	$V_2O_5/g\text{-}C_3N_4$ heterojunction	ST + C	5 μL liquid & 0.03 g catalyst (gas-solid interface)	Visible source (D)	62.4% (~8 h)	31
4	$Bi_2O_3/BiVO_4$ heterostructure	ST + C	3 μL liquid & 0.02 g catalyst (gas-solid interface)	Visible source (D)	70% (~6 h)	32
5	In_2S_3/In_2O_3 heterostructure	HT	5 μL liquid & 0.03 g catalyst (gas–solid interface)	Visible source (D)	76.9% (~8 h)	33
6	In_2O_3@8%PANI composite	HT	5 μL liquid & 0.03 g catalyst (gas–solid interface)	Visible source (D)	82.7% (~8 h)	34
7	BSN–CN heterojunction	US assisted HT + C	60 mL aq. solution (3.3×10^{-5} mol dm^{-3} and 0.1 g catalyst	Visible light broad source (234 mW cm^{-2}); λ = 225 nm; photon flux ~6.5×1014 photons cm^{-2} sec^{-1}	99.9% (~3 h)	Present work

2. Experimental (materials and methods)

2.1. Materials

All reagents used in this experiment were analytical reagent grade (A.R. grade) chemicals from Sigma-Aldrich.

2.2. Synthesis

2.2.1. Synthesis of $Bi_2Sn_2O_7$. The synthesis of bismuth stannate ($Bi_2Sn_2O_7$) was achieved through a hydrothermal process. Aqueous solutions of tin tetrachloride pentahydrate ($SnCl_4{\cdot}5H_2O$) and bismuth nitrate pentahydrate [$Bi(NO_3)_3{\cdot}5H_2O$] were prepared and combined to form a homogeneous mixture after stirring for 30 min and sonicating for 5 min. The pH of the mixture was subsequently adjusted to 14 using a 5 M NaOH solution. The alkaline mixture was then transferred to a Teflon-lined autoclave and heated at 180 °C for 24 h. After cooling, the resulting precipitate was isolated, washed with deionized water and ethanol, and dried at 100 °C to obtain the desired bismuth stannate product. In the manuscript, this will be termed as BSN.

2.2.2. Synthesis of C_3N_5. 5 g of 3-amino-1,2,4-triazole (3-AT) is taken as a precursor, and 5 g of NH_4Cl is added to it and ground to form a heterogeneous solid mixture. This mixture was subsequently subjected to a calcination process at 550 °C for 3 h at a ramp rate of 10 °C min^{-1} under a nitrogen atmosphere to obtain carbon nitride (C_3N_5) as a product. In this manuscript, this will be termed as CN.

2.2.3. Synthesis of $Bi_2Sn_2O_7/C_3N_5$ heterojunction photocatalysts. Different stoichiometries of $Bi_2Sn_2O_7$ were dispersed on C_3N_5 to form heterojunctions through a straightforward ultrasound-assisted hydrothermal method. In a typical synthesis, predetermined quantities of $Bi_2Sn_2O_7$ and C_3N_5 powders were dispersed in 50 mL of ethanol and subjected to ultrasonic agitation for a duration of 20 min. The resulting mixture was then transferred to a 100 mL stainless steel autoclave lined with polytetrafluoroethylene and placed in a vacuum-drying oven at a temperature of 180 °C for 24 h. After cooling to room temperature, the sediment at the bottom was thoroughly washed with deionized water and ethanol, followed by drying in a vacuum-drying oven overnight. The dried product represented the $Bi_2Sn_2O_7$–C_3N_5 heterojunction photocatalyst. Various stoichiometries of $Bi_2Sn_2O_7$ loadings were fabricated to achieve 1, 5, 10 and 15 weight % $Bi_2Sn_2O_7$ over C_3N_5 using the same procedure. This heterojunction will be termed in this manuscript as BSN–CN-1 (for 1 wt%-$Bi_2Sn_2O_7$–g-C_3N_5), BSN–CN-5 (for 5 wt%-$Bi_2Sn_2O_7$–g-C_3N_5), BSN–CN-10 (for 10 wt%-$Bi_2Sn_2O_7$–g-C_3N_5), and BSN–CN-15 (for 15 wt%-$Bi_2Sn_2O_7$–g-C_3N_5), as shown in Scheme 1.

2.3. Characterization

Powder X-ray diffraction (XRD): crystallographic phase analysis was performed using a Philips Analytical diffractometer equipped with Ni-filtered Cu Kα radiation. Diffractograms were recorded within the 10–80° (2θ) range. Transmission electron microscopy (TEM): TEM data were obtained using a 200 kV FEI Tecnai T20 machine. TEM samples were prepared by dispersing powder ultrasonically in alcohol onto a carbon-coated copper grid. Nitrogen adsorption analysis: BET surface area, pore volume, and pore size distribution were determined using a Micromeritics ASAP 2020 analyzer. UV-visible measurements in the 200–800 nm region were performed using a two-beam spectrophotometer (V-670, JASCO) with a diffuse reflectance (DR) attachment, employing barium sulphate-coated integrating spheres as a reference. A Bruker V70V FT-IR (spectral range: 8000 to 50 cm^{-1}; equipped with KBr and multilayer beam splitters and DLTGS and MCT detectors) was employed for the IR absorption detection of the catalysts in the form of a KBr pellet (10 mm diameter, 1.2–1.5 mm thick and 70–100 mg in weight) to record the IR spectra in absorbance mode. To elucidate the electronic states, X-ray photoelectron spectroscopy (XPS) studies were conducted on a SPECS instrument with a PHOBIOS 150 delay line detector (DLD) employing an Al Kα (1483.6 eV) dual anode as the X-ray source (power: 250 W,

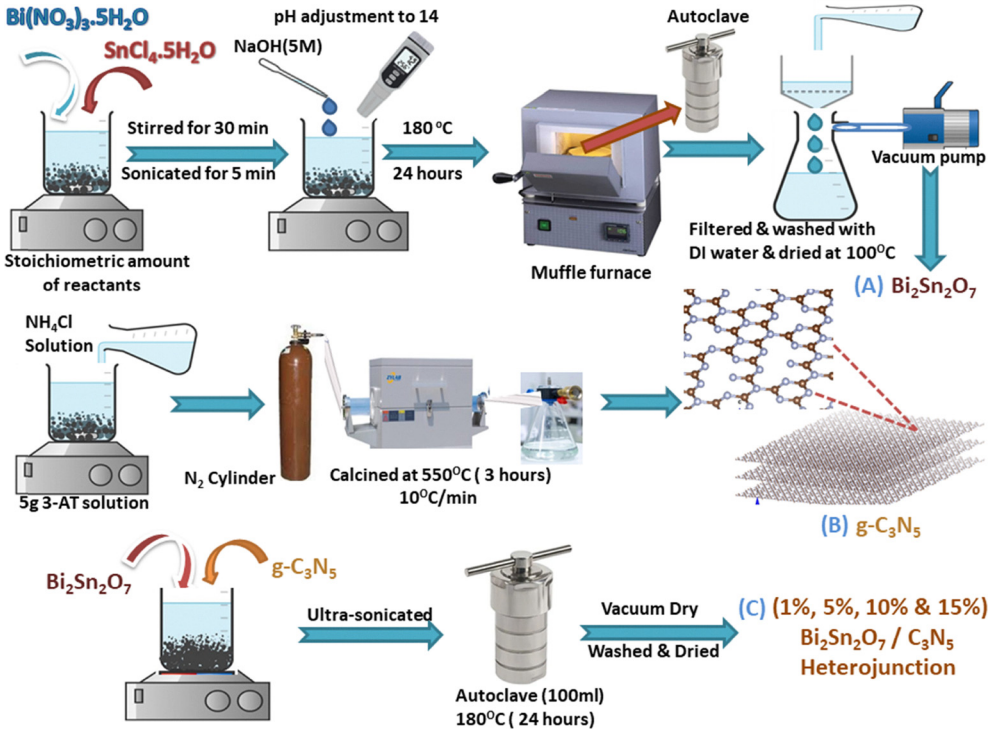

Scheme 1 Hydrothermal synthesis of the CN, BSN and the BSN–CN heterojunction.

voltage: 13 kV, sample current: 175.6 nA) at a pass energy of 50 eV. As an internal reference for the absolute binding energy, the C-1s peak (284.5 eV) was used. All the deconvolutions were carried out using the CASA software with a Voigt type peak having GL (30) without imparting any asymmetry. The baseline was generated using the Shirley function. Zeta potential measurements were performed at 25 °C using a quartz cuvette with a Malvern Zetasizer nanoseries, employing phase analysis light scattering with an applied field strength of 2.5×103 V m^{-1} and a He–Ne laser (632.8 nm) operating at 4.0 mW as the light source. About 0.5 mg mL^{-1} of the sample was dispersed in 1 mL of water. Field emission scanning electron microscopy (FE-SEM) and energy-dispersive spectroscopy (EDS) analyses were conducted using a Carl Zeiss model, GEMINI-SEM300. Mött–Schottky and photo-switching experiments of the semiconductor–electrolyte interface as a function of applied potential were performed with an electrochemical cell connected to a Potentiostat/Galvanostat 2273 for chrono-amperometric switching at a bias of −1.5 V. The cell was irradiated using 1.5 AM sunlight type radiation from an Optosolar solar cell testing system (details in SI). A CHNS(O) analyzer from Thermo Fisher Scientific (model Flash Smart V CHNS/O) was used to determine the percentages of carbon, hydrogen, nitrogen, and oxygen, based on the principle of the "Dumas method", which involves the complete and instantaneous oxidation of the sample by "flash combustion". The combustion products were separated using a chromatographic column and detected by a thermal conductivity detector (TCD), which provides an output signal proportional to the concentration of the individual components of the mixture. The built-in chromatographic column converts the compound and elutes it in the form of NO_2, CO_2, and H_2O, which are then detected using TCD. TRPL measurements were carried out on an Edinburgh FLS-900 instrument equipped with a steady-state 400 W xenon lamp for emission spectroscopy and a hydrogen gas nanosecond lamp (nF920) for lifetime measurements. For superoxide trapping about, 2.5 mg of the photocatalyst was dispersed in 500 μL of water and sonicated for 30 minutes. Then, 10 μL of 5,5-dimethyl-1-pyrroline *N*-oxide (DMPO) was added to the mixture, which was then transferred into a capillary for free radical measurements at room temperature. The EPR spectra were recorded using an X-band Bruker EMX 300 spectrometer, both in the absence and presence of light, at room temperature.

2.4. Photocatalytic activity

Using different loadings of $Bi_2Sn_2O_7$ (1%, 5%, 10% and 15%) in g-C_3N_5, degradation studies of *o*-DCB were carried out. A cylindrical Pyrex glass reactor was used as a photocatalytic reactor for photocatalytic degradation experiments, where the reactor was irradiated perpendicularly with a white light source over the reactor, with the white light source emitting in the 350–700 nm range (flux = 234 mW cm^{-2}) with a peak around 430 nm. The photon flux as measured by a uranyl oxalate actinometer was found to be $\sim 6.5 \times 1014$ photons cm^{-2} s^{-1}. For the photo degradation reaction, 100 mg of a photocatalyst sample was placed in 60 mL of *ortho*-dichloro benzene (*o*-DCB) solution with a molar concentration of 3.3×10^{-5} mol dm^{-3} (pH ~6). The photocatalytic systems were stirred for 5 min at 200 rpm to disperse the powders, as BSN–CN is sparingly soluble in aqueous media. Next, the systems were placed under the visible lamp. After every 10 min of visible-light exposure,

one aliquot of *o*-DCB solution was taken, and the absorbance was measured using a UV-Vis spectrophotometer. Similarly, the other mixtures were subjected to stirring for 10 min. Next, the optical absorption measurement of the supernatant was carried out on a JASCO UV-670 spectrophotometer at the wavelength λ = 225 nm, which corresponds to a maximum in the absorption spectrum of the *o*-DCB solution. As a result, different sets of BSN–CN catalysts demonstrated excellent photocatalytic activity for the degradation of *o*-DCB. Almost complete or partial degradation was achieved within 180–290 minutes for many of the catalyst formulations. The unique heterojunction formed between $Bi_2Sn_2O_7$ and C_3N_5, coupled with the tunable bandgap, contributed to the enhanced photocatalytic performance. The results indicate the potential of $Bi_2Sn_2O_7$ doped C_3N_5 catalysts for effective *o*-DCB degradation.

2.5. Electrospray ionization-mass spectrometry (ESI-MS) study

In this study, we conducted an experimental analysis of the BSN–CN set of catalysts to compare their photocatalytic activity for the oxidation of *ortho*-dichlorobenzene (*o*-DCB). This investigation is essential for understanding the reaction kinetics and identifying different intermediates formed during the oxidation of *o*-DCB, leading to the production of carbon dioxide, using a diverse set of catalysts. ESI-MS studies were carried out using a Thermofisher Q Exactive plus Orbitrap mass spectrometer equipped with an electrospray ionization source. The molecular masses (*m*/*z*) were determined directly by injection at a flow rate of 5 uL min^{-1} through the ion source operated in positive mode. The capillary temperature (for desolvation) was maintained at approximately 320 °C. The ion spray voltage was maintained at 3.5 kV. The samples were introduced after dilution to a concentration range of 2–10 μM using ESI-MS grade water and filtered through 0.2 μm filters. The acquisition time was two minutes with five microscans being recorded.

For the *ex situ* ESI-MS study, 60 mL of the *o*-DCB aqueous solution with a molar concentration of 0.14 M was placed in a beaker and each photocatalyst (100 mg) was added. The photocatalytic system was initially stirred for 20 min at 200 rpm in the dark to disperse the powders for adsorption analysis. Subsequently, the systems were exposed to visible light. At every 10-minute interval, a portion of *o*-DCB solution was withdrawn and diluted with water to make a final concentration of 5 μM, and the resulting peaks were measured using an *ex situ* ESI-MS instrument. The same stirring procedure was repeated for the other mixtures, with the ESI-MS peak measured after 10 minutes of stirring. Notably, complete degradation of *o*-DCB was observed in ~180 minutes when BSN–CN-15 was used as the catalyst, while for other catalysts—BSN, CN, BSN–CN-1, BSN–CN-5, and BSN–CN-10—partial/complete degradation of *o*-DCB was observed in ~180 to 290 minutes.

3. Results and discussion

3.1. X-ray diffraction (XRD)

Shannon *et al.* reported that α-$Bi_2Sn_2O_7$ (BSN) transforms to β-$Bi_2Sn_2O_7$ above 410 K.[35] XRD peaks at 14.4, 23.6, 24.66, 27.76, and 36.6 suggest the formation of the tetragonal BSN phase (α form) at room temperature.

In contrast to ideal pyrochlores, which adopt a cubic structure, Bi has a coordination number of 5 and Sn exhibits an octahedral coordination. The BiO_5 – pentahedra is attached to the SnO_6 – octahedra by corner sharing only, and a small amount of edge sharing results in a very complex structure, as has been hypothesised by many groups recently, in which the unit cell consists of 176 atoms.[36] The different planes for the $Bi_2Sn_2O_7$ are shown in the Fig. 1B(a), representing the $Bi_2Sn_2O_7$ with C1c1 ICSD-239965 indicating mainly α-$Bi_2Sn_2O_7$. The synthesised g-C_3N_5 (CN) displays a sharp diffraction peak at around 2θ = 27.28° (002), which suggests a layered structure with a specific interlayer spacing (d_{002}) typical of g-C_3N_5. Therefore, the samples produced were mostly composed of g-C_3N_5.[37,38]

The low-angle peak at 13.2° can be assigned to an in-plane structural motif that predicts the difference between the adjacent polymer units and is not seen, which is natural for the synthesised C_3N_5 at a higher temperature of 500 °C. The intensity of the peak at 27.28° decreases as a function of BSN dispersion, and there is a slight shift in the peak to form the heterojunction structure, showing the BSN to be present and dispersed between the graphitic layers. However, at room temperature there are no signature XRD peaks related to BSN, even at 15 wt% dispersion. Once the BSN–CN-15 is heated at around 180 °C (Fig. 1B(b)), it shows peaks for BSN, and becomes highly crystalline at ~750 °C (Fig. 1B(e)). This clearly proves that the BSN is present with the CN in the BSN–CN heterojunction and is mostly present in the surface or between the layers.

A thorough Rietveld refinement was carried out to understand the lattice parameters and the strain in the lattice for the BSN–CN-15 samples upon heating (Fig. S13 and S14). As understood from Fig. 1B, the concentration and crystallinity of BSN increases in the BSN–CN-15 upon heating at different temperatures. The strain factor also increases upon increasing the BSN concentration in the BSN–CN-15 samples treated at higher temperature as observed from the Table 3. Similarly, in Fig. 1A in the different BSN–CN materials, the concentration of BSN increases in the BSN–CN heterojunction. Therefore, the strain should increase as a function of BSN concentration in BSN–CN in a similar fashion, as shown in Table 3.

3.2. Morphological studies (HR-TEM, FE-SEM, elemental mapping and SAED studies)

A. HR-TEM and crystallographic understanding. HR-TEM (Fig. 2) for the BSN–CN catalyst is important for understanding this material, as the XRD does not show a crystalline BSN phase with CN at room temperature. The HR-TEM images of BSN–CN-15 and that of BSN–CN-1 show definite fringes, which are resolved to show the BSN planes of (400) and (404), respectively, clearly showing the presence of the nano crystalline BSN in the BSN–CN heterojunction.

The inset of Fig. 2A shows the SAED pattern of the BSN–CN-15, as presented in Table S3, clearly showing the crystalline pattern of BSN present over the CN, thereby proving the formation of the heterojunction. Similarly, in Fig. 2B the SAED pattern of the BSN–CN-1 shows a definite crystalline pattern of BSN (presented in

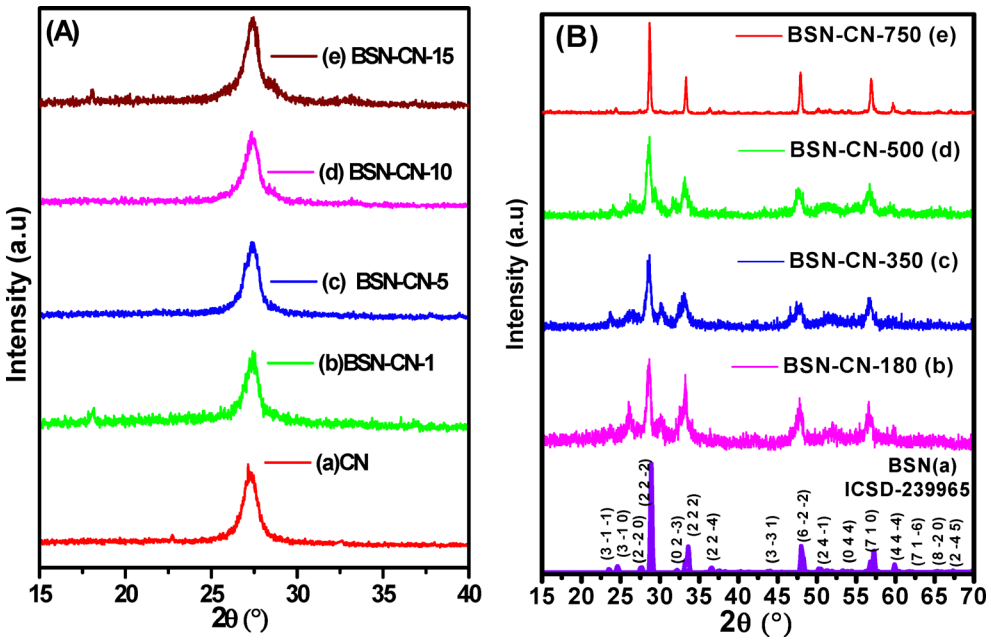

Fig. 1 (A) XRD for the different samples: (a) CN; (b) BSN–CN-1; (c) BSN–CN-5; (d) BSN–CN-10; and (e) BSN–CN-15. (B) XRD of the BSN–CN-15 as a function of temperature: (a) BSN; (b) 180 °C; (c) 350 °C; (d) 500 °C; and (e) 750 °C.

Table S4 in the SI), also clearly showing the formation of nano crystalline BSN over CN, thereby effectively proving the formation of the BSN–CN heterojunction in BSN–CN-1. Even the *d*-spacing calculation matches with that of the (400) (Fig. 2A) and the (404) plane (Fig. 2B), thereby also showing the formation of nano crystalline BSN. Variation in the particle size was observed in the different TEM images, as shown in Fig. 2C–F. The BSN synthesised by the same route (Fig. 2C) shows a particle size around ~15–18 nm, and CN also shows a particle size of ~97–100 nm (Fig. 2D). However, in the heterojunctions formed there is an increase in the particle size as a function of the dispersion of the BSN over the CN. The BSN–CN-5 has a particle size of ~115 nm (Fig. 2E) and BSN–CN-15 has a particle size of ~145 nm (Fig. 2F).

B. FE-SEM and elemental mapping with EDS studies. The FE-SEM images for the different samples are shown in Fig. 3. The CN sample shows a typical ridge-like structure for the g-C_3N_5, as has been observed earlier in the literature.[39] The FE-SEM images of BSN show typical granular structures, which are aggregates of small irregular nanoparticles.[40] Slight alteration in particle surface morphology between CN and heterojunction samples is observed, which indicates that metal species were homogeneously dispersed on the CN support. The elemental mapping for the BSN–CN heterojunction shows the elements to be present in the same places showing clear formation of the BSN–CN heterojunction. The EDS data and the elemental mapping confirm the presence of CN and BSN (Table S1). The EDS data strongly support the presence of Bi and O, Sn, C and N in the heterojunction.

3.3. DR-UV-Vis studies

An estimate of the optical band gap energy (E_g-gap) was obtained from a plot of the Kubelka–Munk function $F(R)$ as given below in eqn (1):[41]

$$F(R) = A(h\nu - E_g)^{m/2} \quad (1)$$

where $h\nu$ is the photon energy and m is a constant that depends on the nature of the optical transition. For a direct transition, the value of m is 1 (if allowed) or 3 (if forbidden), while for indirect transitions, m is 4 (if allowed) or 6 (if forbidden). For a weakly absorbing semiconductor, $F(R)$ is proportional to the absorbance, A. Hence, the energy intercept of a plot of A^2 (for direct allowed transition) or $A^{1/2}$ (for indirect allowed transition) *versus* $h\nu$ yields the corresponding optical band gap, E_g, when the linear region is extrapolated to the zero ordinate. The band gap of BSN was found to be 2.90 eV, a bit higher than that reported in earlier literature.[8] It is classified as an indirect band gap material, and based on the density of states, the valence band (VB) is principally composed of O-2p and Bi-6s orbitals, hybridized with Sn-4d orbitals. The conduction band (CB) is primarily composed of Bi-6p, Sn-5s, and a partial admix of O-2p orbitals.[42] The hybridized states of the VB and CB predominantly demonstrate the involvement of Sn-5s and Bi-6s orbitals, suggesting a high degree of mobility for the photo-induced electron density. The blueshift in the band gap can be attributed to the quantum confinement effect owing to a smaller particle size of hydrothermally synthesized BSN particles as reflected in the TEM section. The band gap of the synthesized CN is 2.36 eV (Fig. 4B), which matches with the earlier literature.[13,43] The composites synthesised by the hydrothermal route possess band gaps within 2.36 eV (Fig. 4), and there is a systematic reduction in the band gap of CN as a function of BSN dispersion percentage. These heterojunctions show band gap values of 2.34 eV (BSN–CN-1), 2.25 eV (BSN–CN-5), 2.17 eV (BSN–CN-10), and 2.07 eV (BSN–CN-15), as shown in Table 2. This observed decrease in the band gap energy may be

attributed to a combination of factors including the formation of a heterojunction at the interface between BSN and CN, the introduction of defect states within the CN structure, and alterations in the material's morphology and crystal structure induced by BSN dispersion. The XRD results, as shown earlier, do not show a complete change in the material morphology and crystal structure. Critically, this narrowing of the band gap enhances the photocatalytic activity under visible-light irradiation by enabling the material to absorb a broader range of lower-energy photons, thereby increasing the efficiency of light harvesting. Furthermore, the creation of a heterojunction facilitates efficient charge separation by promoting the transfer of photogenerated

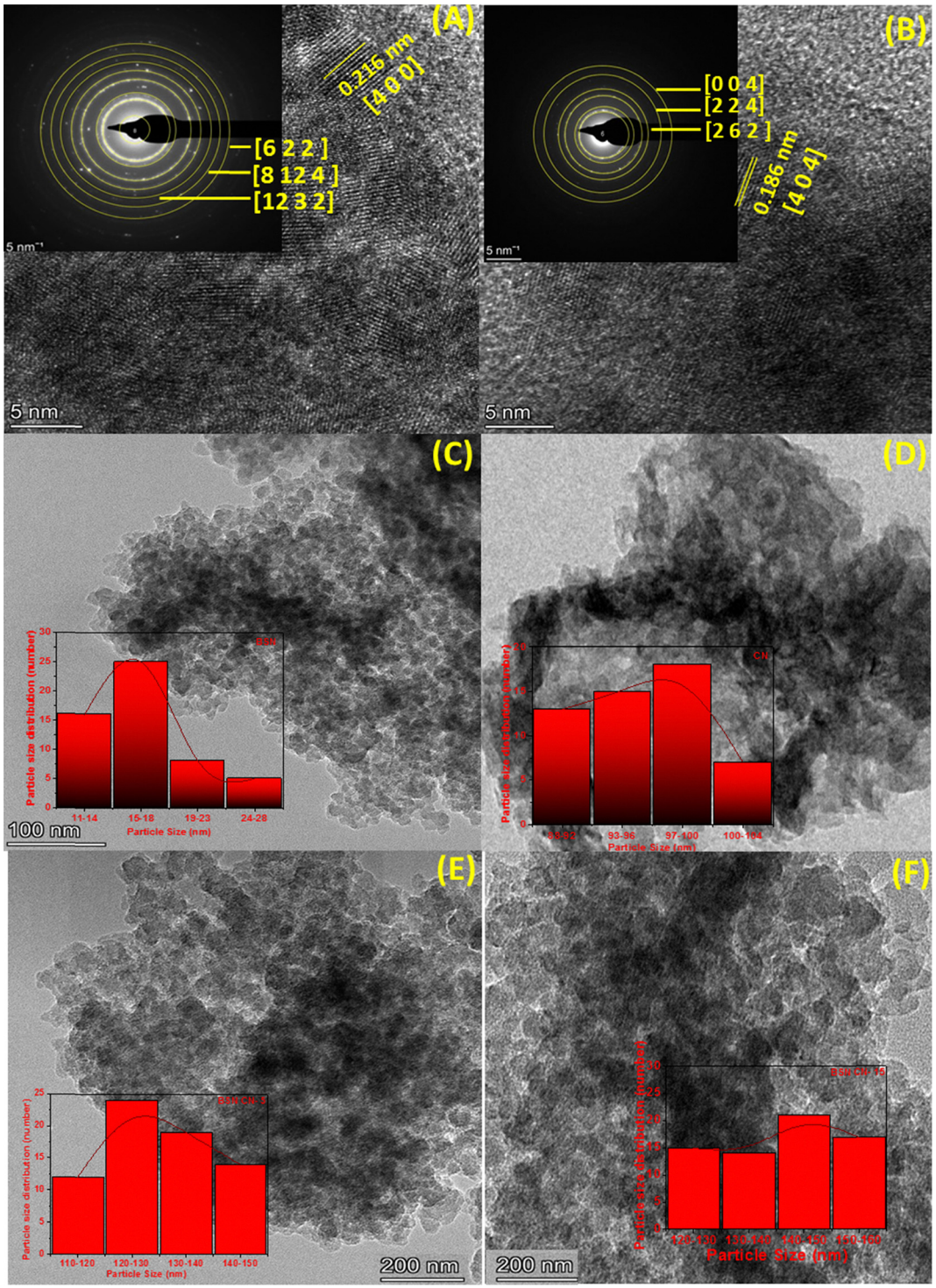

Fig. 2 HR-TEM and TEM images for the different samples: (A) BSN–CN-15; (B) BSN–CN-1; (C) BSN; (D) CN; (E) BSN–CN-5; and (F) BSN–CN-15. The insets in (A) and (B) show the respective SAED patterns and the insets in (C) to (F) show the particle size distributions.

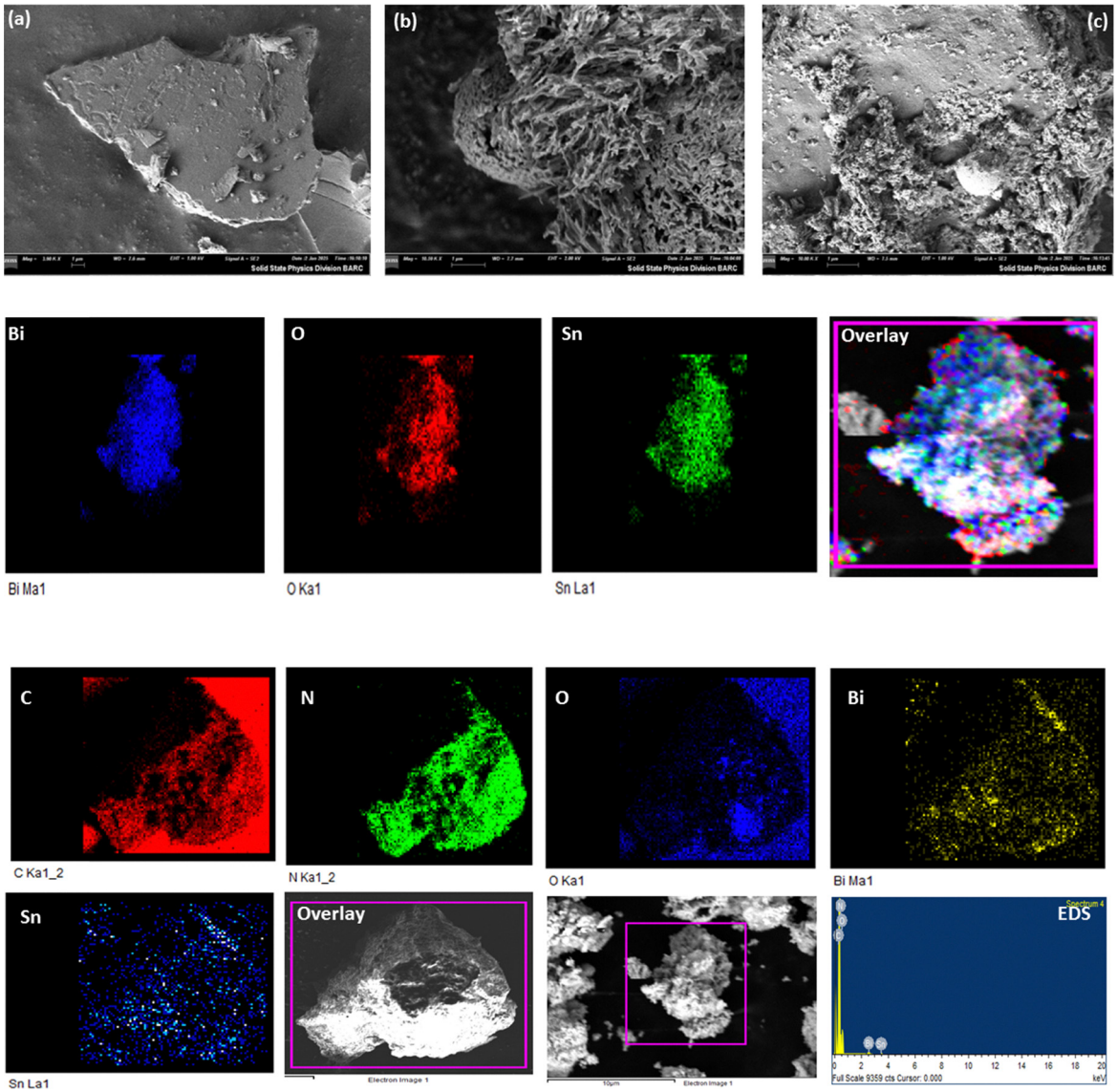

Fig. 3 (A) The first row represents FE-SEM micrographs for the different samples: (a) BSN; (b) CN; and (c) BSN–CN-15. (B) The second row shows elemental analysis with EDS data showing elements Bi, Sn and O, and their overlay for the BSN sample. (C) Third and the fourth row represents elemental mapping for the BSN–CN shows elements C, N, O, Bi, and Sn, and their overlay, and the related FE-SEM image. The final image of fourth row shows the EDS results showing the different elements obtained.

electrons and holes between the two constituent materials, effectively mitigating electron–hole recombination and thereby increasing the availability of charge carriers (electrons and holes) to drive redox reactions on the material's surface, ultimately leading to a substantial improvement in the overall photocatalytic performance, specifically within the visible-light region of the electromagnetic spectrum.

The band gap of the BSN–CN heterojunction decreases as a function of the dispersion of BSN. The band gap of the heterojunction depends on structural factors such as: (a) particle size: the particle size varies as a function of the BSN dispersion in the BSN–CN-heterojunction as observed in the TEM studies (Fig. 2), showing an increase in the particle size (Fig. 5B). The band gap decreases with an increase in the particle size, and the red shift is mainly due to the reversal of the quantum confinement effect.[5] (b) Effect of strain: as shown in the XRD section, with an increase in the BSN concentration in the BSN–CN heterojunction the lattice strain increases. The higher lattice strain is reflected in the lower band gap value for a higher concentration of BSN in the BSN–CN heterojunction. (c) Effect of charge exchange from the space charge layer: the band gap of a heterojunction decreases if the space charge layer increases, leading to strong upward band bending, which is the case for the BSN–CN heterojunction. The BSN–CN mainly forms a Schottky heterojunction, and the difference in the charge separation increases as a function of BSN in the BSN–CN heterojunction, which is evidenced later in XPS studies. This clearly shows the increase in the space charge barrier, which reduces the VB potential, as has been calculated from the Mött–Schottky experiment (Scheme 2). The increase in the space

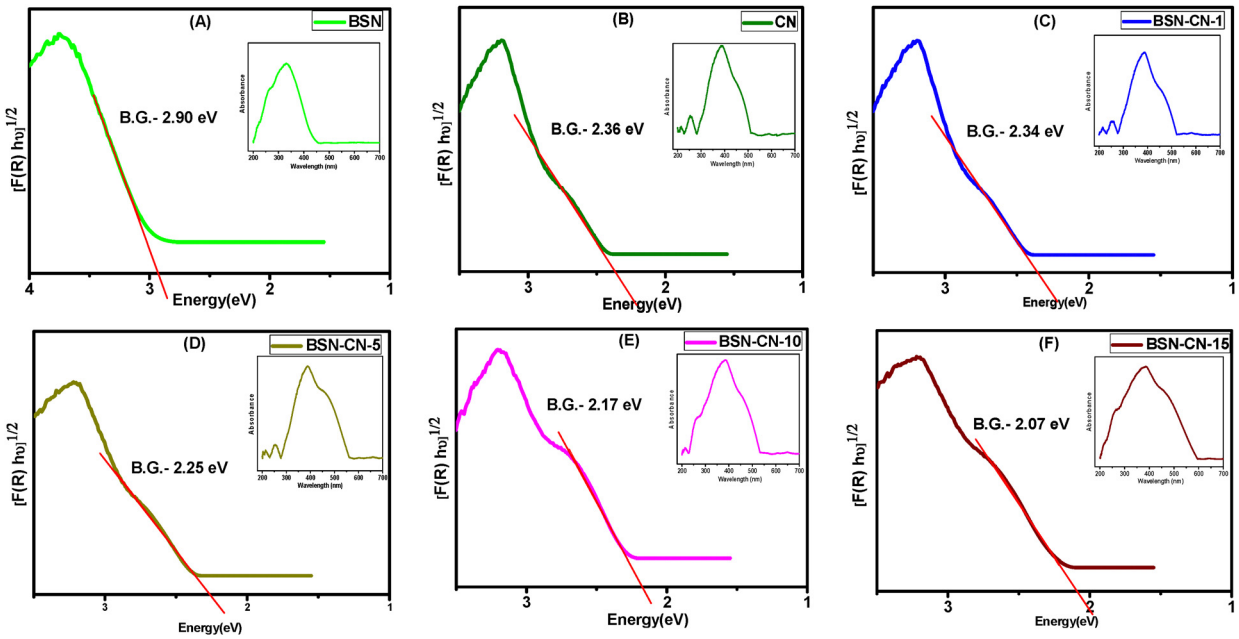

Fig. 4 Kubelka–Munk plots for the different samples, with the insets showing DR-UV-Vis spectra for the photocatalysts: (A) BSN; (B) CN; (C) BSN–CN-1; (D) BSN–CN-5; (E) BSN–CN-10; and (F) BSN–CN-15.

charge usually decreases the band gap, as observed for the BSN–CN heterojunctions.

To further validate the involvement of superoxide as the active oxygen species, 5,5-dimethyl-1-pyrroline *N*-oxide (DMPO) was employed as a spin-trapping agent. As depicted in Fig. 5A, EPR spectra exhibited distinct DMPO–$O_2^{\bullet-}$ adduct peaks[23,44] under light irradiation, whereas no such peaks were observed in the dark. This result unequivocally confirms the generation of superoxide radicals ($O_2^{\bullet-}$) and suggests a sequential two-electron step. Fig. 5A(c) clearly shows the formation of the DMPO–$O_2^{\bullet-}$ adduct peaks for the BSN–CN-15, which are not that prominent for either CN (Fig. 5A(b)) or BSN (Fig. 5A(a)), showing the effective formation of the heterojunction, which facilitates electron conduction, thereby favourably forming superoxide radicals ($O_2^{\bullet-}$).

3.4. X-ray photoelectron spectroscopy studies (XPS)

High-resolution spectra of C-1s and N-1s were further deconvoluted into Gaussian–Lorentzian peaks (Fig. 6A and B). The deconvoluted C-1s pattern of CN shows significant contributions at binding energies (BE) of 284.5 eV and 286.6 eV, and 287.5 eV and 288.2 eV (Fig. 6A(a)). The first peak can be assigned to the presence of graphitic carbon (or adventitious C), and the next two correspond to sp^2 carbon in nitrogen-bearing aromatic rings (N–C═N) and C–N bonds, respectively. The final peak corresponds mostly to C–N (where the N is a quaternary amine), thereby substantially lowering the electron density over C.[13] In conjunction with the previous literature, the N-1s spectrum (Fig. 6B(a)) can be deconvoluted into 3 main signals located at BE of 398.2 eV, 399.3 eV and 400.7 eV, corresponding to pyridinic N in a heptazine ring (C–N═C), pyrrolic nitrogen (from a triazole moiety) and overlap of quaternary nitrogen [N–$(C)_3$]/secondary amine species, respectively.[11–14] Li *et al.* have described them as associated with C═N–C, C–N═N–C (C–NH_2), and π electron delocalization (π–π*), respectively.[45,46] Upon formation of the BSN–CN composite, there is an alteration in the electron density around both C and N for the CN, as reflected in the XPS data of C-1s and N-1s for these samples. In the C-1s, there are smaller changes in the binding energy for the CN–BSN composite. In the BSN–CN-5 onwards, the sp^2 carbon in nitrogen is shifted slightly to a higher BE of 0.2 eV; however, there is a definite change in the N-1s peak of quaternary N of 401.2 eV, which is shifted to a lower BE of 400.6 for BSN–CN-5 onwards (Fig. 6B), showing a probable electronic interaction. There is a definite systematic shift in the N-1s peak to lower BE as a function of the BSN in the BSN–CN heterojunction, showing an increase in the electron density around N-1s. The negative charge around N-1s increases systematically as a function of BSN in the BSN–CN heterojunction. The Bi-4f (Fig. 6C) shows two prominent peaks, after l-s coupling corresponding to binding energies of 158.8 eV (Bi $4f_{7/2}$) and 164.1 eV (Bi $4f_{7/2}$) for the BSN catalyst, consistent with the previous literature.[47]

Table 2 Crystallite size, textural properties, band gap data and isoelectric points

S. no.	Samples	Isoelectric point[a] (eV)	Band gap[b] (eV)	BET surface area[c] ($m^2\ g^{-1}$)	C/N ratio[d]
1	BSN	8.64	2.90	18	—
2	CN	6.78	2.36	50	0.652
3	BSN–CN-1	7.51	2.34	12	0.678
4	BSN–CN-5	6.72	2.25	8.1	0.682
5	BSN–CN-10	6.26	2.17	4.5	0.678
6	BSN–CN-15	5.50	2.07	2.7	0.652

[a] Isoelectric point calculated from the zeta potential vs pH plot (Fig. 8). [b] Band gap values calculated from the Kubelka–Munk (KM) function of the DR-UV plot. [c] Calculated from N_2-adsorption studies (BET) for microporous materials. [d] C/N ratio calculated using the CHN analyser.

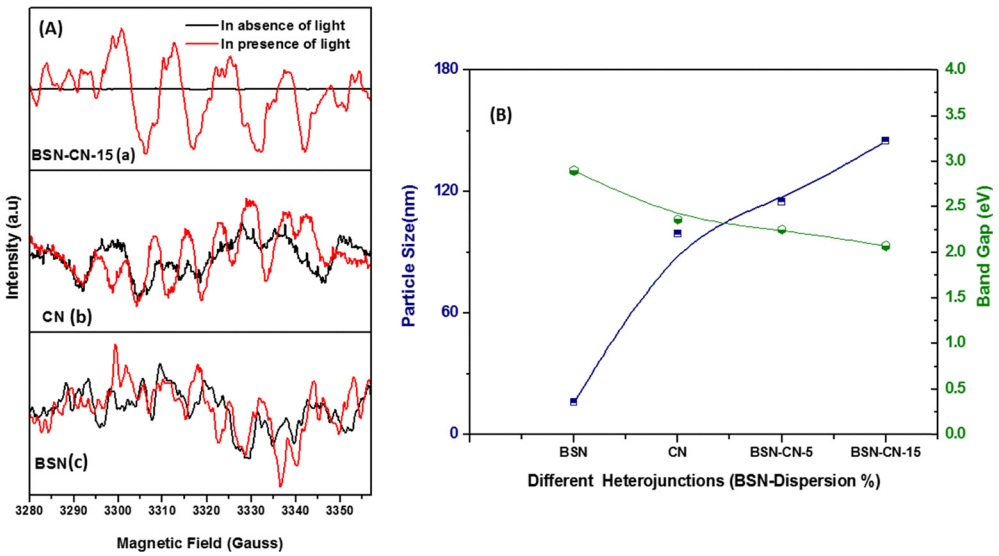

Fig. 5 (A) Electron paramagnetic resonance (EPR) detection of DMPO–$^{\bullet}O_2^-$ over different catalysts: (a) BSN–CN-15; (b) CN and (c) BSN. (B) Variation of particle size (from TEM studies) and bandgap (from Kubelka–Munk studies) with increasing dispersion of BSN.

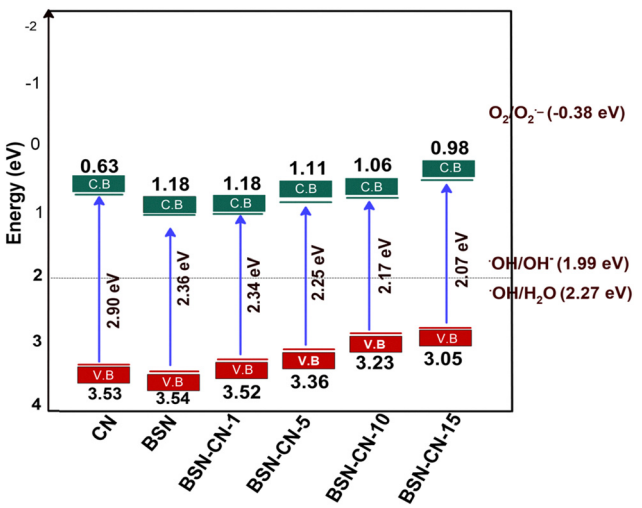

Scheme 2 The different valence band potentials and the conduction band potentials for the CN, BSN and set of BSN–CN photocatalysts.

However, for the different composite materials, there is a slight shift in the binding energy towards a higher BE. The Bi $4f_{7/2}$ of BSN–CN-1 exhibits a BE of 159 eV, and that of the BSN–CN-15 has a BE of 159.6 eV, which shows there is definitely a depletion of the electron density around Bi due to the formation of the BSN–CN composite. There is a systematic increase in the BE of the Bi as a function of BSN increase in the BSN–CN heterojunction, showing more depletion of electron density from the Bi. The Sn-3d XPS spectra can be deconvoluted to Sn-$3d_{5/2}$ (490.9 eV) and Sn-$3d_{3/2}$ (499.36 eV) with a $\Delta\varepsilon$ of 9.6 eV, which matches with the earlier literature.[48] No alteration in the binding energy of the Sn for the BSN–CN composites formed (Fig. 6E) shows no change in the electron density around Sn of the BSN for the composite formation. The O-1s XPS spectra for the BSN can be deconvoluted into three peaks with BE at 529, 532 and 533 eV.[49]

The first peak mainly represents the O-lattice, the second represents the surface-OH and the third represents the O-vacancy.[2,3] There is a definite alteration in the electron density around O, which can be correlated with BSN–CN composite formation. There is a definite increase in the BE of the lattice O and a decrease in the BE of the O-vacancy showing that the lattice O and the O-vacancy present over the surface react electronically due to the formation of the BSN–CN nano composites.

3.5. FT-IR analysis

The Fourier transform infrared (FT-IR) spectra of the synthesized catalysts (Fig. 7) were meticulously analyzed to gain deeper insights into their surface functional groups and bonding interactions, which play a crucial role in their photocatalytic performance. The set of peaks in the range 1100–1500 cm^{-1} is mainly due to the C=N and C–N bond stretching vibrations (Fig. 7B(e)), and a broad signal between 2700 and 3600 cm^{-1} is assigned to H–X (X = N, O) stretching of amino groups and hydroxyl groups (Fig. 7A(e)). A strong peak around 803 cm^{-1} in all the samples indicates out-of-plane bending vibrations of N-containing heterocyclic (triazine/tri-*s*-triazine) rings (Fig. 7B(e)).[50] This is attributed to C–N stretching vibrations of the typical 1–3-*s*-triazine cycles, and its intensity was found to decrease with the dispersion or BSN–CN composite formation. This might indicate the formation of carbon vacancies upon composite formation, thereby reducing the structural integrity of the 1–3-*s*-triazine cycles to a certain extent.[37] The absence of a characteristic peak at 650 cm^{-1} for *s*-triazine indicates that the polymers are composed mainly of tri-*s*-triazine type units. The peaks at 1234 and 1320 cm^{-1} are due to the bridging secondary amine groups attached to aromatic rings.[51] C–N stretching vibrational bands appeared at 1252, 1323 and 1402 cm^{-1}.[52,53] The band at

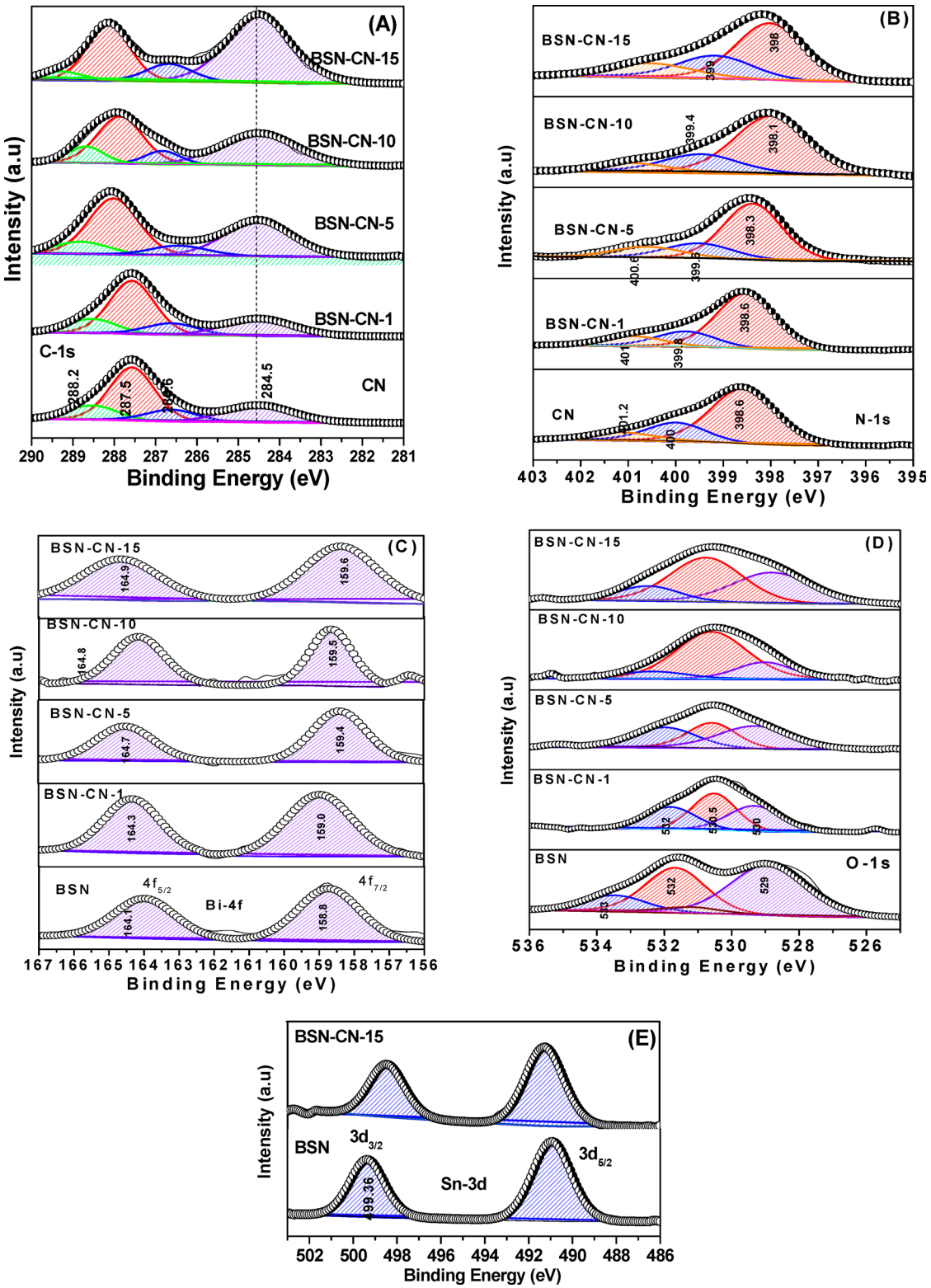

Fig. 6 Deconvoluted XPS spectra for (A) C-1s, (B) N-1s, (C) Bi-4f, (D) O-1s, and (E) Sn-3d for the different samples: (a) CN; (b) BSN; (c) BSN–CN-1; (d) BSN–CN-5; (e) BSN–CN-10; and (f) BSN–CN-15.

1633 cm^{-1} is related to C=N stretching vibration modes.[54] The absorption band at 3420 cm^{-1} originates from the water molecules, while the stretching mode of N–H appeared at 3200 cm^{-1}, showing incomplete condensation.[55,56] In the FT-IR spectra for the BSN sample, in the bending region, the absorption bands at 610 cm^{-1} were due to Sn–O stretching. The vibrations in the

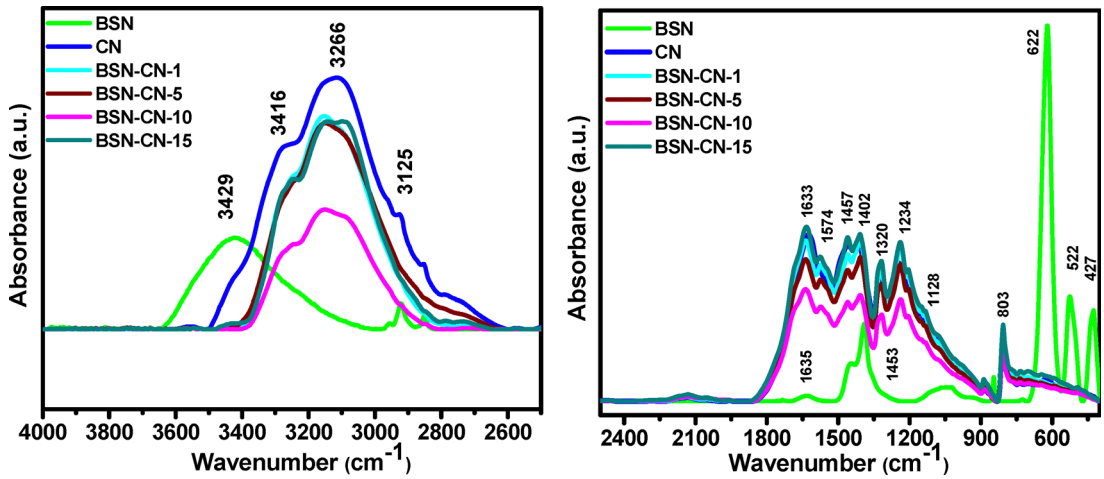

Fig. 7 FT-IR spectra for the different samples: BSN; CN; BSN–CN-1; BSN–CN-5; BSN–CN-10 and BSN–CN-15.

SnO_6 octahedron and the B–O are stretching vibration modes of BSN,[19] whilst the weak bending bands at 530 and 427 cm^{-1} are ascribed to Bi–O–Bi bond vibrations.[57] The bands centered at about 3415 cm^{-1} and 1630 cm^{-1} are assigned to O–H stretching and bending modes of water, respectively.

The FT-IR of the different composites/heterojunctions also shows vibrational bands in the stretching region (4000–2800 cm^{-1}). A prominent and broad peak centered around 3400 cm^{-1} was consistently observed across all samples. As discussed earlier, this characteristic peak is attributed to the stretching vibrations of O–H groups, indicating the presence of adsorbed water molecules and/or surface hydroxyl groups (–OH). The broadness of the peak suggests a range of hydrogen bonding interactions. The intensity and shape of the O–H peak varied significantly with the BSN content in the heterojunctions. For example, for CN, the major peak as suggested earlier is at 3416 cm^{-1}, exhibiting a specific intensity and shape, and similarly for the BSN sample, the –OH peaks were observed at 3429 cm^{-1}. However, the BSN–CN composites show -OH groups mainly at 3416 cm^{-1} with notable changes in the intensity of the different bands as a function of the concentration of BSN in CN. These variations strongly suggest alterations in the surface hydroxylation state of the materials. Surface hydroxyl groups are known to play a vital role in photocatalysis by influencing the adsorption of reactant molecules and participating in the generation of reactive oxygen species (ROS), such as hydroxyl radicals ($^{\bullet}OH$), which are primary oxidants in the degradation of organic pollutants like *o*-DCB. The peaks at 3266 and 3125 cm^{-1} in CN can be tentatively assigned to N–H stretching vibrations and vary noticeably with BSN concentration, showing a definite interaction between the BSN and the NH of CN. Therefore, using this along with the XPS data, it can be concluded that these BSN–CN materials clearly show electronic interactions and are heterojunction composites. In the lower wavenumber region (2000–400 cm^{-1}), more complex and characteristic spectral features were observed. However, it is important to note that adsorbed water molecules can also contribute to peaks in this region. The region below 1000 cm^{-1} is particularly informative for identifying the presence of metal–oxygen bonds. The increasing intensity of the metal–oxygen peaks with higher BSN loading confirms the increasing presence of BSN in the heterojunction-composite materials.

3.6. Zeta potential

The zeta potential serves as a crucial parameter for finding the effective surface potential established by the electrical double layer at the interface in the BSN–CN set of photocatalysts in a solvated aqueous environment. Considering the photocatalytic degradation of *o*-DCB in water as an essential solid–liquid interphase reaction, any alterations in the surface charge of the photocatalyst will exert a considerable influence on both the adsorption process and the subsequent evolution of various intermediate species during photo-oxidation. The evaluation of the zeta potential (Fig. 8B) will provide surface interaction details for the BSN–CN heterojunction as a function of the pH. At neutral pH (pH-7), CN shows a negative surface charge (Fig. 8B(a)), whereas BSN shows a positive surface charge (Fig. 8B(b)). The surface charge initially decreases for BSN–CN-1 and BSN–CN-5 as compared to CN, and starts increasing with a higher percentage of BSN. The BSN–CN-10 and BSN–CN-15 has positive surface charge mostly reflecting the effect of the BSN in the heterojunction. At lower pH, there is an addition of H^+ to the system, and typically, the surface charge should increase, which is more or less reflected in the zeta potentials of these photocatalysts. Under alkaline or basic conditions (pH ~10), there is a greater amount of OH^- on the surface and therefore, the surface charge should be lower than that at pH 7. Consistently, all these photocatalysts possess a negative surface charge at pH ~10 (Fig. 8B). This supports the trend of increasing negative surface charge with increasing pH.

The data suggest that the point of zero charge (PZC) of the BSN–CN system is likely around pH 7, where the zeta potential changes sign. In conclusion, the zeta potential data reveal that the stability of the BSN–CN is highly dependent on pH and dispersion percentage. pH 10 appears to be the most favourable for achieving a stable dispersion. This information is valuable for optimizing the preparation and application of this catalyst system. The values of the isoelectric point are presented in Table 2.

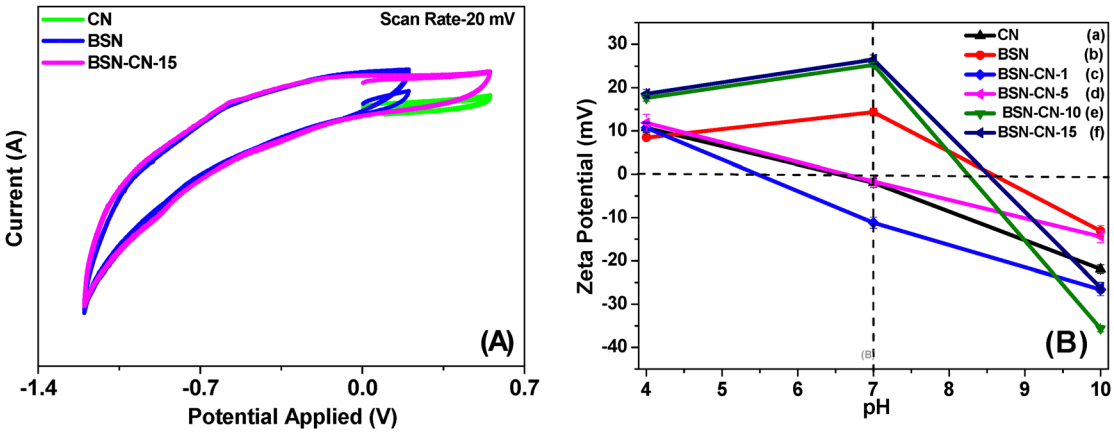

Fig. 8 (A) Cyclic voltammetry data for the different samples: (a) CN; (b) BSN; and (c) BSN–CN-15. (B) Plot of zeta potential as a function of pH for the different samples: (a) CN; (b) BSN; (c) BSN–CN-1; (d) BSN–CN-5; (e) BSN–CN-10; and (f) BSN–CN-15. The zeta potential data show statistical error bars for average errors for a number of repetitions.

3.7. Cyclic voltammetry (CV)

The cyclic voltammograms (in terms of the current density) in the 200 to 500 mV region for the CN show the characteristic features of g-C_3N_5.[58] With a higher scan rate, the hysteresis of the curve increases (Fig. S8). However, the CV features for the BSN at a scan rate of 20 mV (Fig. 8A(b)) show that the electrochemical features are different from those of the CN. The BSN–CN-15 (Fig. 8A(c)) shows a completely different CV as compared to that of CN and that of BSN. This shows that there is definite electronic interaction between the two, and, in conjunction with the XPS and FT-IR data, it confirms the formation of the heterojunction of the CN and BSN. Cyclic voltammetry (CV) is an electroanalytical technique used to study redox reactions by sweeping the electrode potential and measuring the resulting current. It is a powerful tool for characterizing electrochemical systems, providing insights into their redox potential. A heterojunction's capacitance–voltage (*C–V*) curve differs from that of its constituent materials (parents) because it reveals: (a) band discontinuities: when two dissimilar semiconductors form a heterojunction, their band gaps and band alignments at the interface are discontinuous. This creates a unique energy band structure at the interface that dictates the behavior of charge carriers. (b) Altered carrier transport: the presence of an internal electric field at the heterojunction interface leads to superior charge separation and improved transport of electrons and holes. This enhanced charge transfer, often seen as a synergistic effect, is a key feature of heterojunctions and is reflected in their CV measurements. (c) Enhanced charge separation at the junction interface or in the space charge region. The alteration in the CV of the heterojunction, therefore, shows clearly the space charge separation in the BSN–CN heterojunction formation and the band bending as shown in Scheme 3.

3.8. Mött–Schottky and photovoltaic switching and experiment

Mött–Schottky (MS) analysis has been widely adopted in the field to estimate key operational parameters of semiconductor photo electrodes, namely the flat band potential, E_{fb}, and the donor concentration, N (for an n-type semiconductor photoanode), or acceptor concentration, Na (for a p-type photocathode). The Mött–Schottky relationship shows the apparent capacitance measurement as a function of potential under depletion conditions (eqn (2)):

$$\frac{1}{C^2} = \frac{2}{e\varepsilon\varepsilon_0 N}\left(E - E_{fb} - \frac{kT}{e}\right) \quad (2)$$

where C = capacitance of the space charge region; ε = dielectric constant of the semiconductor; ε_0 = permittivity of free space; N = donor density (electron donor concentration for an n-type semiconductor or hole acceptor concentration for a p-type semiconductor); E = applied potential; E_{fb} = flatband potential; k = Boltzmann constant; T = temperature; and e = electronic charge.

The donor density can be calculated from the slope of the $1/C^2$ *vs.* E curve, and the flat band potential can be determined by extrapolation to $1/C = 0$.

The model required for the calculation is based on two assumptions:

(a) Two capacitances must be considered: the capacitance related to the space charge region (C_{sc}) and the double layer (C_{dl}) are considered in series. As $C_{dl} \gg C_{sc}$, the contribution of the double layer capacitance in this total capacitance is almost negligible. Therefore, the capacitance value calculated from this model is assumed to be mainly the value of the space charge capacitance.

(b) The equivalent circuit used in this model is a series combination of a resistor and a capacitance (the space charge capacitance). The capacitance is calculated from the imaginary component of the impedance [Im(Z)] using the following relationship (eqn (3)):

$$\mathrm{Im}(Z) = \frac{-1}{2\pi fc} \quad (3)$$

This model is adequate if the frequency (fc) is high enough (in the order of kHz).

In the Mött–Schottky plot, eqn (2) (plot of the $1/C^2$ *vs.* E) showing a negative slope corresponds to a p-type

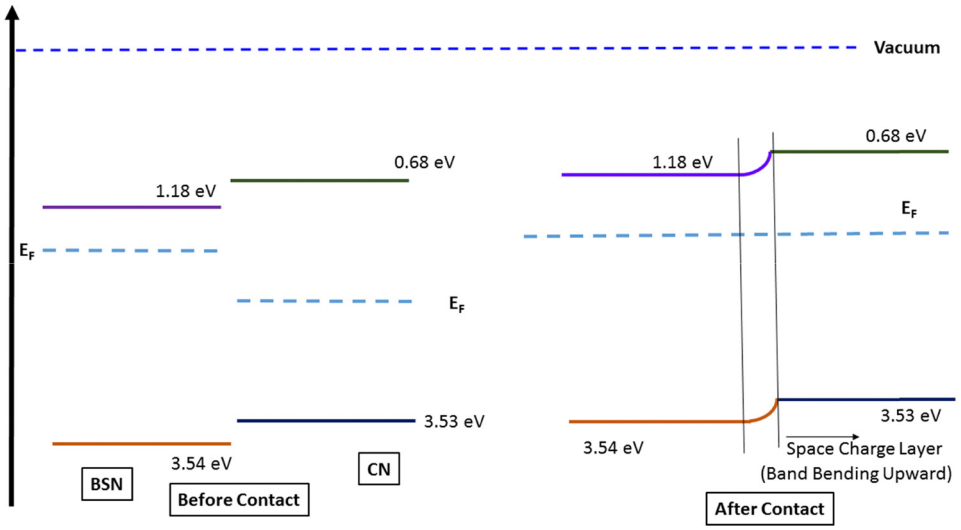

Scheme 3 Formation of a space charge layer and band bending after the formation of the heterojunction.

semiconductor (mainly hole acceptor), and a positive slope to an n-type semiconductor (an electron carrier). The intercept of this plot at $C = 0$ will provide the value of the flat band potential for the material.

Mött–Schottky analysis of the CN and BSN/CN shows negative slopes (Fig. 9A) in the $1/C^2$ *vs.* voltage plots, and therefore, it can be confirmed that they are p-type semiconductors with mainly electrons as the dominant charge carriers. However, as materials like CN and BSN will have different Fermi energies, these materials are entirely different, and the values of their "ε" and "ε_0" are also different; therefore, the slope value of each of them will not exactly relate to their respective donor densities (N). However, the flat band potential (E_{fb}) has been calculated for all these systems from the intercept in eqn (2). The valence band potential can be calculated from the E_{fb} calculation for E_{KCl} (0.1 M) to SHE (pH-7) to SHE (pH-0) to vacuum:

(1) E_{KCl} (0.1 M) to SHE (pH-7) = 0.2881 V.

(2) SHE (pH-7) to SHE (pH-0) = 0.414 V.

(3) SHE (pH-0) to vacuum = 4.5 V (vacuum).

Therefore, for the valence band potential:

$$E_{VB} = [E_{fb} - (0.414 + 0.2881 - 4.5)] \quad V = (E_{fb} + 3.7979)\ V \tag{4}$$

$$E_g = (E_{VB} - E_{CB})V \tag{5}$$

So,

$$E_{CB} = (E_{VB} - E_g)V \tag{6}$$

The E_{VB} values calculated from the Mött–Schottky plots are given in Scheme 2.

Importantly, a clear trend of decreasing slope with increasing BSN concentration was observed, signifying an increase in carrier concentration. This observation suggests that the incorporation of BSN into CN leads to a higher density of free electrons, which can be attributed to two primary mechanisms: (a) electron donation: BSN may act as an electron donor to CN, directly increasing the number of free electrons in the composite material. This electron transfer could stem from the difference in Fermi levels between BSN and CN, driving electrons from BSN to CN. (b) Defect generation: the introduction of BSN could create defect states within the CN structure, either through lattice mismatch or interfacial interactions. These defects can act as electron traps or donors, effectively increasing the electron concentration in the material. Furthermore, a subtle shift in the flat band potential was observed with increasing BSN concentration. This shift implies that BSN influences the band bending and energy level alignment in CN, potentially creating a heterojunction for charge separation and transfer. The electronic interaction found with the XPS, FT-IR and CV results previously, therefore, confirms that a heterojunction between BSN and CN is supported by the observed changes in carrier concentration and flat band potential. As the BSN content increases, the interface between BSN and CN expands, leading to a larger heterojunction area. This expanded heterojunction facilitates more efficient charge separation and transfer due to the built-in potential at the interface. The different values of the calculated valence band potential and that of the conduction band potential using the band gap value are shown in Scheme 2. The photovoltaic switching (switch-on/off experiments) behavior of the synthesized catalysts, encompassing BSN, CN and different heterojunction composites of BSN–CN, was investigated to elucidate their photo-responsive properties, directly relevant to their photocatalytic efficacy. The cyclic current–time plots (Fig. 9B) demonstrate a clear and reversible resistive switching behavior across all samples, indicating the materialfs ability to generate and modulate photocurrent upon visible-light irradiation. The photo-switching experiments show the photocatalysts of BSN to possess maximum photocurrent density as compared to that of the CN. Similarly, the BSN–CN composites also show good photo-response currents and can be considered very good photocatalysts.

Scheme 2 shows a systematic increase in the VB potential as a function of BSN dispersion in the BSN–CN heterojunction. The BSN–CN heterojunction, while visually similar to typical

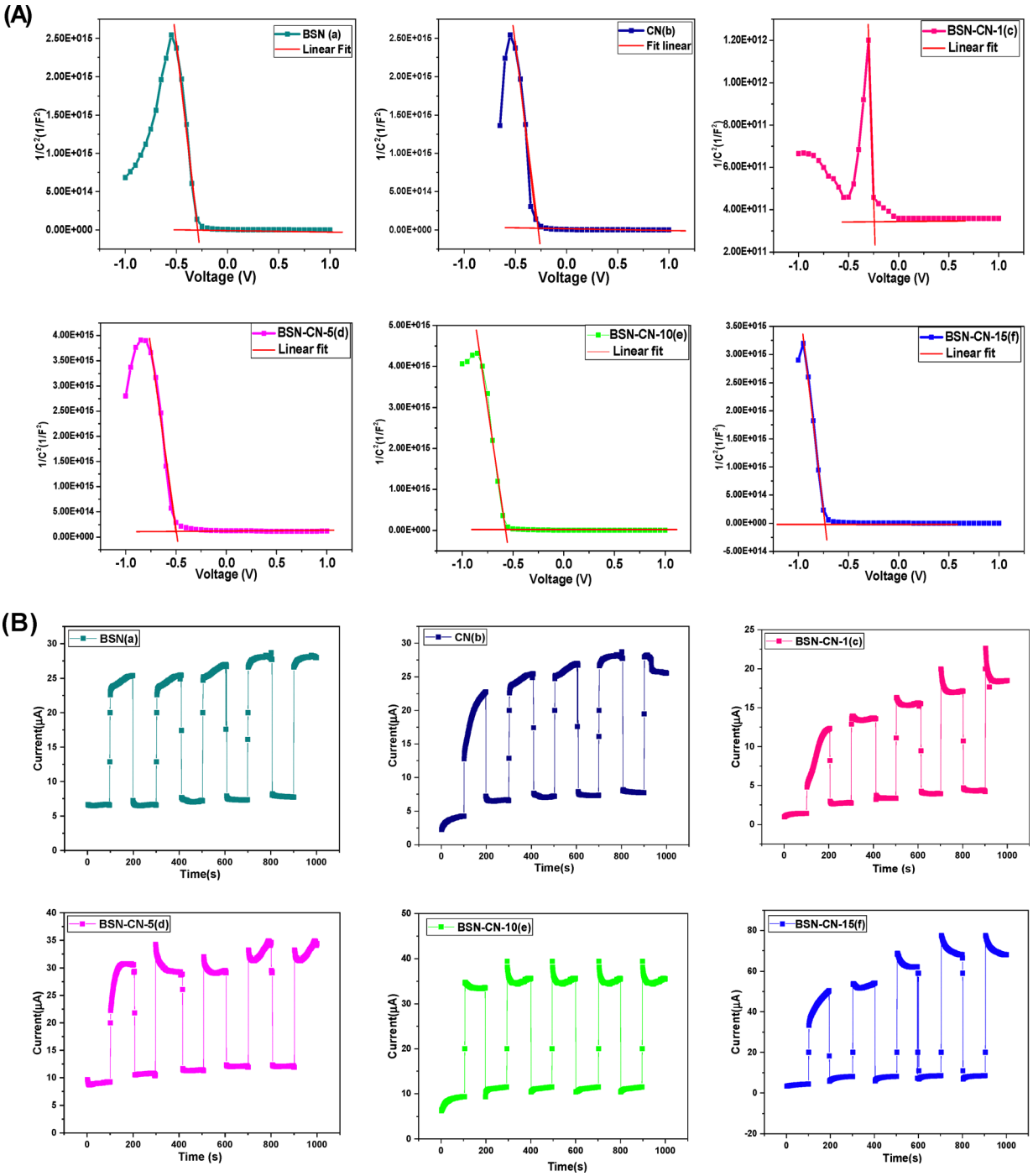

Fig. 9 (A) The first two rows depicts Mött–Schottky and (B) the last two rows shows photo-switching data for the different samples: (a) BSN; (b) CN; (c) BSN–CN-1; (d) BSN–CN-5; (e) BSN–CN-10; and (f) BSN–CN-15.

van der Waals systems with its sheet-like structure, functions with a more powerful mechanism: a Schottky barrier. The formation of this barrier stems from the natural misalignment of the Fermi energy levels between BSN and CN. This mismatch is a critical factor, as it drives a much higher degree of charge separation than that found in simple van der Waals junctions. This increased charge separation is directly responsible for a process called band bending at the valence band (VB) and conduction band (CB) interfaces. Our XPS data provide concrete evidence of this phenomenon, showing a distinct charge separation around the Bi-4f and N-1s orbitals in the BSN–CN heterojunction. A systematic increase in positive charge around Bi-4f and a corresponding increase in negative charge around N-1s were observed with increasing BSN concentration. This progressive charge separation is a clear signature of an S-scheme heterojunction in action. The resulting band bending,

which is directly affected by the increased charge splitting of the Schottky barrier, leads to a noticeable lowering of the valence band. This effect is meticulously detailed in Scheme 2, where we illustrate the alteration of the BSN–CN VB. While Schottky barriers are more commonly seen at semiconductor–metal interfaces, their presence here at a semiconductor–semiconductor interface is driven by the significant Fermi level mismatch between BSN and CN, as confirmed by our Mött–Schottky studies (Fig. 9A). Ultimately, the robust charge separation that results from the alignment of these Fermi regions is the key to the superior performance of the BSN–CN photocatalyst.[59–61] With g-C_3N_5 being a p–n-type material, its Fermi level mostly lies between the VB and the CB,[62,63] and with BSN being a p-type material, its Fermi level lies near to its CB,[64] and accordingly, the Schottky barrier is represented in Scheme 3.

3.9. Photoluminescence (PL) and time-resolved-photoluminescence (TRPL) data

Steady-state photoluminescence (PL) at 375 nm excitation and time-resolved photoluminescence study for CN, BSN and BSN–CN photocatalysts were carried out. Fig. 10A shows the corresponding emission spectra for CN and the different heterojunction samples as a function of the dispersion of BSN over the CN samples. These CN samples were synthesized at 500 °C and possess a typical PL band around 469 nm. Graphitic materials usually possess a PL band at 430 nm due to fast recombination of photo-excited electron–hole (excitons) pairs radiatively.[65] However, the PL band for the CN at 469 nm (Fig. 10A(e)) can be ascribed to thermally induced incorporation of defects in CN–X structures, which contribute to the PL process and are present within the band gap of the materials.[66] The defect level mostly lies below the LUMO and hence requires lower energy than the radiative recombination process, which causes a red-shift. However, for the BSN the PL emission observed is very low as compared to that of the CN materials and also from the literature.[19] In the reported study, BSN was synthesized using a citrate precursor method and subjected to calcination at 800 °C, whereas our samples were prepared with only a mild heat treatment at 100 °C. This significant difference in thermal processing likely results in a higher defect density in the reported samples, which may enhance their photoluminescence (PL) properties, compared to our BSN samples. In the CN–BSN heterojunction, the photoluminescence (PL) intensity decreases consistently with increasing proportion of BSN in the heterojunction. Notably, BSN–CN-15 exhibits the lowest PL emission, confirming that the formation of the heterojunction alleviates the recombination of photogenerated electron–hole pairs.[19,67] The lower the PL emission, the less the recombination of the photo-excited holes and electrons, and the better the photocatalytic activity, as shown in the next section.

The luminescence decay profiles for all the different heterojunction samples, along with CN, are shown in Fig. 10B. All of these can be fitted with only a bi-exponential function, as shown in eqn (7):

$$I(t) = I_0 + B_1 \exp\left(\frac{-t}{\tau_1}\right) + B_2 \exp\left(\frac{-t}{\tau_2}\right) \quad (7)$$

where I_0 is the background or zero offset, τ_1 and τ_2 are the two lifetimes, and B_1 and B_2 are pre-exponential factors, as shown in Table 4.

The deviation from direct exponential decay and the presence of multiple lifetimes has been documented previously in the literature for carbon nitride-based materials.[13,16] A lower lifetime (~2 s) is mostly attributed to the photogenerated charge carrier recombination from anti-bonding (σ* and π*) to bonding π molecular orbitals[68] and a higher lifetime is ascribed to non-radiative transitions like inter system crossing (ISC) from σ* to π*, as well as defect levels.[69] In the case of heterojunctions, the lifetime τ_2 (ns) and the comparative B2 increase, making the average lifetime of these materials more than that for CN. The time-resolved results for the BSN, despite repeating a number of times, were not that stable for our system. Therefore, it is clear that the heterojunction exhibits a longer lifetime leading to lower PL and better photocatalytic activity.

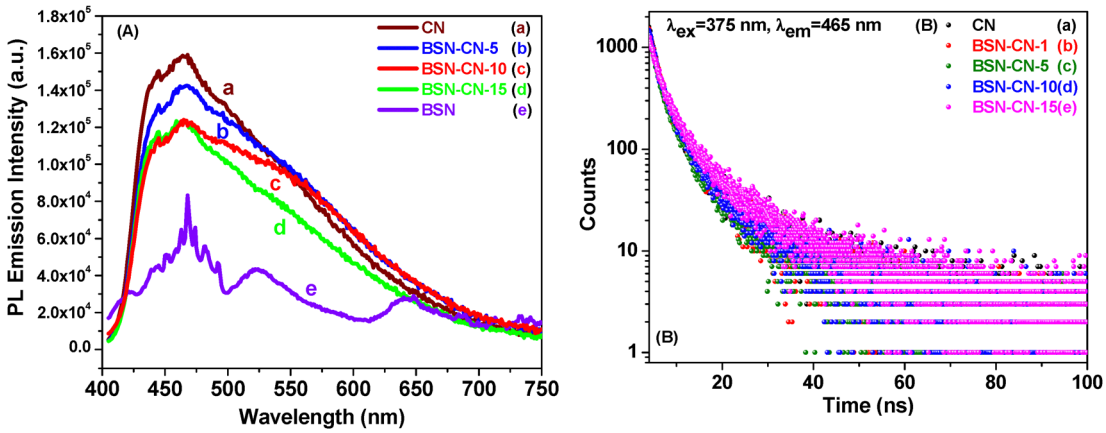

Fig. 10 (A) Photoluminescence data for the different samples: (a) CN; (b) BSN–CN-5; (c) BSN–CN-10; (d) BSN–CN-15; and (e) BSN. (B) Photoluminescence lifetime data for the different samples: (a) CN; (c) BSN–CN-1; (d) BSN–CN-5; (e) BSN–CN-10; and (f) BSN–CN-15.

3.10. CHN analysis

Elemental carbon-to-nitrogen (C/N) ratios were considered, as determined by CHN analysis, to understand the structure of the C_3N_5. The pristine carbon nitride (CN) sample exhibited a baseline C/N ratio of 0.652, reflecting the C_3N_5 structure as has been reported earlier,[70,71] which is much greater than the C/N ratio of g-C_3N_4. The elemental analysis from the XPS data set also shows a $C(sp^2)$: N ratio of 3 : 4.9. The C/N ratios for the different composites of BSN–CN remain almost comparable and are shown in Table 2. Therefore, the structure of the C_3N_5 is not compromised by the formation of the BSN–CN composites. The surface elemental analysis for the C : N ratio for the different composites from XPS also reflects a similar understanding. Therefore, the CHN analysis, along with the elemental analysis from XPS, shows that with the formation of the heterojunction, the CN structure remains intact.

3.11. Photocatalytic activity

The photocatalytic activity of the synthesized BSN–CN samples was assessed through the degradation of *ortho*-dichlorobenzene (*o*-DCB), a model organic pollutant, under visible-light irradiation. The experimental details regarding the irradiation source were provided earlier. Notably, all the catalysts had band gaps in the range of 2.90 to 2.07 eV, which lie in the visible region. *Ex situ* ESI-MS spectroscopy was employed as a complementary technique to elucidate the nature of the photocatalytic intermediates formed during *o*-DCB degradation, thereby serving as a proof-of-concept for the reaction mechanism.

Fig. 11A depicts the variation in photocatalytic activity of the synthesized materials as a function of % BSN in CN. The detailed kinetic data for the individual photocatalysts are presented in Fig. S2–S7. It is crucial to note that the self-degradation of *o*-DCB in the absence of a photocatalyst is negligible (Fig. S1). Consequently, the percentage of degradation products is calculated using eqn (8).

The product percentage (PC%) is

$$\mathrm{PC}(\%) = \frac{C_o - C_i}{C_o} \times 100 \qquad (8)$$

where C_o = UV-Vis intensity of the *o*-DCB without any catalyst and C_i = UV-Vis intensity of *o*-DCB without the particular photocatalyst at time t_i.

In order to achieve a quantitative understanding, the catalytic performance activities for the different photocatalysts are shown in the inset of Fig. 11A, showing a plot of $t_{1/2}$ *vs.* the % dispersion of the BSN–CN lattice.

Table 4 Individual and average PL data for photogenerated charge carriers in heterojunction samples having different percentages of BSN

Catalyst	τ_1 (ns)	B_1	τ_2 (ns)	B_2
CN	2 (59.5%)	1360	10.8 (40.5%)	171
BSN–CN-1	2 (57.9%)	1220	9.4 (42.1%)	195
BSN–CN-5	2 (63.4%)	1460	9.4 (36.6%)	187
BSN–CN-10	2.1 (61%)	1490	9.8 (39%)	203
BSN–CN-15	2.48 (59.3%)	1260	11.98 (40.7%)	179

The absence of *o*-DCB self-degradation during the experiment confirms its stability under visible irradiation from the lamp. The enhanced visible-light photocatalytic activity for *o*-DCB degradation is attributed to the modulation of the electronic band structure of the pyrochlores induced by varying the % dispersion of BSN in CN. Notably, BSN–CN-15 exhibited the highest activity (~99.9% degradation in 180 minutes, rate constant $k = 38.38 \times 10^{-3}$ min^{-1}, $t_{1/2}$ = 18.06 min). In comparison, the synthesized catalysts, BSN, CN, BSN–CN-1, BSN–CN-5 and BSN–CN-10 displayed degradation efficiencies of 30% (290 min, $k = 1.23 \times 10^{-3}$ min^{-1}), 36% (275 min, $k = 1.62 \times 10^{-3}$ min^{-1}), 80% (270 min, $k = 5.96 \times 10^{-3}$ min^{-1}, $t_{1/2}$ = 116.28 min), 93% (210 min, $k = 11.08 \times 10^{-3}$ min^{-1}, $t_{1/2}$ = 62.54 min), and 99.9% (210 min, $k = 21.93 \times 10^{-3}$ min^{-1}, $t_{1/2}$ = 31.6 min), respectively. The recyclability of the BSN–CN-15 is shown in Fig. S12 for four consecutive cycles. It shows a slight decrease in the catalytic efficiency of the catalyst as a function of recyclability to the extent of 81.4% for three hours of photocatalytic reaction under similar conditions. The catalyst is treated after reaction at 100 °C for 2 h. This leads to an enhancement of the degradation percentage of *o*-DCB solution to ~85% in 3 h. CN, BSN and BSN–CN-15 were used for the photocatalytic degradation of *o*-DCB with a closed photocatalytic reactor (Fig. S9), and the parameters of the products were estimated with a mass spectrometer, as explained in the supplementary information. The product from each was found to be CO_2, and the percentage CO_2 was calculated according to eqn (S12) in the SI. The percentage of product (CO_2) formation is shown in Fig. 11B, where it is shown that the BSN–CN-15 is the most active catalyst, forming ~99% CO_2 in 180 min.

3.12. *Ex situ* ESI-MS study for the intermediates

Ex situ electron spray injection-mass spectrometry (ESI-MS) was employed to elucidate the photocatalytic degradation mechanism of *o*-DCB over the synthesized catalysts, including BSN, CN, and their heterojunction composite BSN–CN-15, by identifying the reaction intermediates formed during the process.

Table 3 Unit cell parameters of BSN–CN-15 heated at different temperatures

	Lattice parameters[a]			Bond angle in unit cell[a]		
Sample	*a*	*b*	*c*	$\alpha = \beta$	γ	Strain (calculated)[b]
BSN–CN-15-350 °C	12.25 (0.01)	7.67 (0.01)	14.90 (0.02)	90	123.8	1.83×10^{-4} (8.2×10^{-6})
BSN–CN-15-500 °C	15.07 (0.02)	9.61 (0.14)	16.58 (0.02)	90	127.82	16.5×10^{-4} (8.2×10^{-5})
BSN–CN-15-750 °C	13.08 (0.004)	7.56 (0.003)	15.14 (0.005)	90	125	21.0×10^{-4} (2.9×10^{-6})

[a] Calculated from the Rietveld refinement. [b] Calculated from the Williamson–Hall equation (Fig. S15).

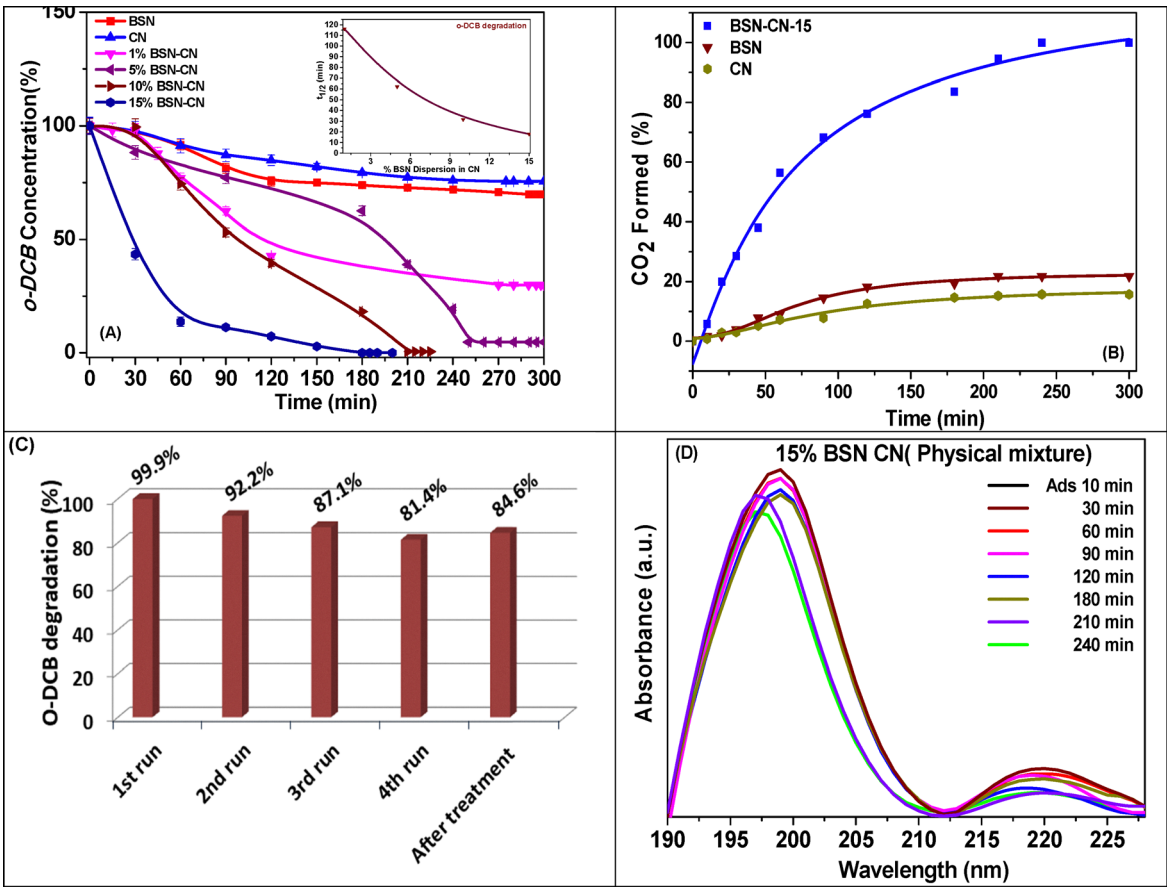

Fig. 11 (A) Photocatalytic activity for mineralization of *o*-DCB by different catalysts: (a) BSN; (b) CN; (c) BSN–CN-1; (d) BSN–CN-5; (e) BSN–CN-10; and (f) BSN–CN-15. The inset shows the change in $t_{1/2}$ as a function of dispersion of BSN over CN. (B) Percentage of CO_2 formation (final product) as a function of time using different photocatalysts using mass spectroscopy: (a) BSN–CN-15; (b) BSN; and (c) CN. (C) Recyclability for the *o*-DCB degradation under similar conditions using BSN–CN15. (D) UV-Vis spectra for the degradation of *o*-DCB solution using a 15% BSN and CN physical mixture.

Fig. 12A presents the ESI-MS spectra of pure *o*-DCB and *o*-DCB in aqueous solution, serving as a baseline for comparison. The spectrum of pure *o*-DCB revealed characteristic mass peaks corresponding to its molecular ion and associated fragments, while the aqueous solution spectrum indicated potential interactions with water molecules, possibly leading to minor shifts or changes in peak intensities.

A. *o*-DCB water solution. The mass spectrum of *o*-DCB mainly shows mass fragments of 146, 111, 75 and 50 (*m*/*z*). However, the *o*-DCB solution shows 159 and 160 as the main peak with a very strong peak at 110 representing catechol. Therefore, the photocatalytic degradation of this mixture involves the degradation of *o*-DCB + H_2O and catechol together.

B. BSN. Fig. 12B displays the ESI-MS spectra of the *o*-DCB solution in water degradation over the BSN photocatalyst at various time intervals (30, 90, 180, 240, and 290 minutes). As the reaction progressed, a gradual decrease in the intensity of the *o*-DCB peaks was observed, accompanied by the emergence of new peaks, indicating the formation of intermediate products. These intermediates are crucial for understanding the degradation pathway. The peaks for the different mass spectra are considered up to the intensity of 1.0×10^7 in order to understand the intermediates.

Peaks that are obtained at 30 min are at *m*/*z* of 58, 69, 74, and 110, along with very minor peaks at *m*/*z* of 159 and 160. There are quite minor peaks observed at *m*/*z* of 87 and 89. The peak at *m*/*z* of 58 represents acetone and that at 69 acetic acid. The mass peak at *m*/*z* of 74 represents either benzene, butanol or an ester of CH_3–O–COO–C_2H_5 known as a McLafferty ion.[72] However, the ester has minor fragmentation peaks at 87 and 89, which are observed during the reaction, confirming the mass peak at 74 to be that of esters. The other peak for the mass spectra at *m*/*z* of 69 represents acetic acid. After 180 min, if we consider the *m*/*z* with an intensity of 2×10^6, there are several new peaks that are obtained. One is at *m*/*z* of 98 with fragmentation at 65 and 66 representing phenol.[73] Other smaller peak intensities with *m*/*z* of 88 correspond to an ester as suggested above, and there is also a strong peak at *m*/*z* 120, again suggesting the McLafferty rearrangement. However, as a function of time the intensities of the intermediates of acetone, catechol and the ester decrease (Fig. 13). The degradation intermediates and plausible mechanism are depicted in Scheme 4. Fig. 13 shows the degradation of the different intermediates as a function of time.

C. CN. Fig. 12C displays the ESI-MS spectra degradation of *o*-DCB solution in water over the BSN photocatalyst at various

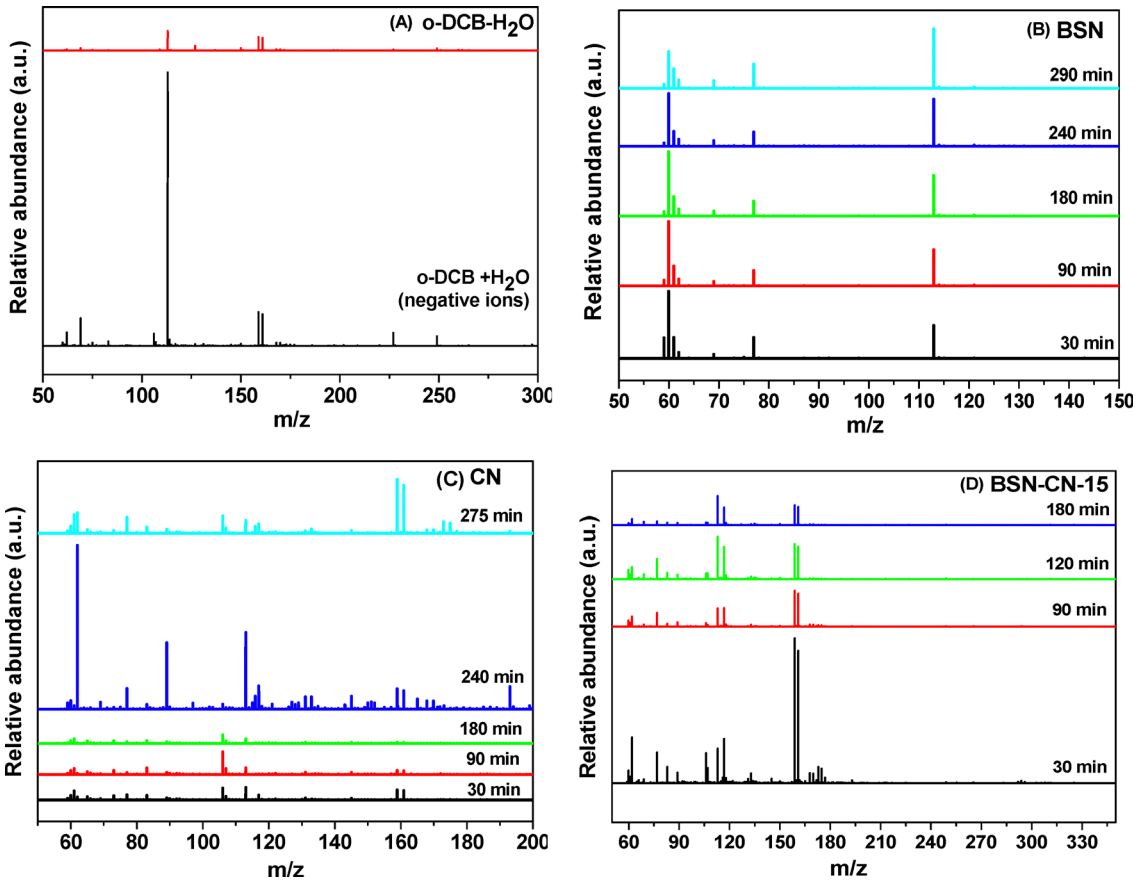

Fig. 12 ESI-MS spectra for the degradation products of the different photocatalysts: (A) *o*-DCB + H_2O mixture; (B) BSN; (C) CN; and (D) BSN–CN-15; in order to understand the different intermediates formed over the catalytic surfaces.

time intervals (30, 90, 180, 240, and 275 minutes). The intermediates formed for degradation of the *o*-DCB by this photocatalyst are not the same as those of the BSN (Fig. 14). The different peaks observed after 30 min of irradiation are at *m*/*z* values at of 58, 59, 60 and 62, representing acetone. There is a peak with a lower intensity at *m*/*z* of 64, mostly representing a dimer of Cl.[35] There are then several peaks at *m*/*z* values of 68, 69, 72, 74, and 76, and the *m*/*z* of 72 represents ethyl butanal, an aliphatic aldehyde.[58] The peak at 74, discussed earlier in the case of BSN, is accompanied by the peaks at *m*/*z* of 68 and 69, representing the McLafferty ion ester of CH_3–O–COO–C_2H_4.[74] There are a few peaks at *m*/*z* of 88, 105, 106 and 112. The peak at *m*/*z* 112 represents catechol and the previous two are mass fragments of catechol. The peak at *m*/*z* of 88 generally corresponds to 2-pentanol or the fragment of an ester. When we observe mass peaks at an intensity of 2×10^7, there are certain peaks that will be observed more for the intermediates, as the intensity is quite low.

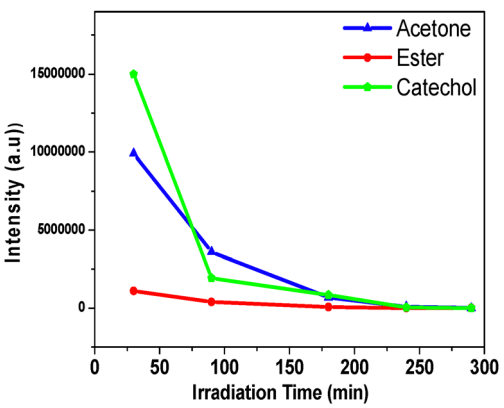

Fig. 13 Variation of the intensities in the mass spectra of the major intermediates as a function of time for the BSN photocatalyst.

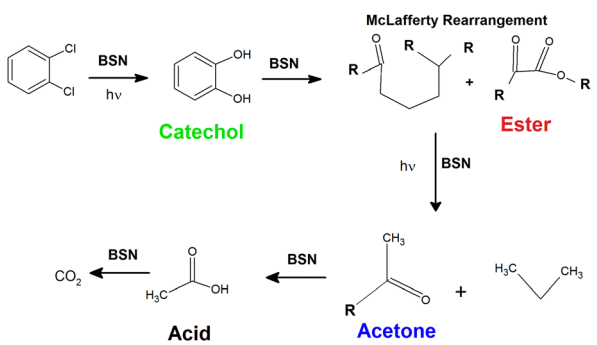

Scheme 4 Plausible intermediates formed by the BSN photocatalyst from the ESI-MS data set.

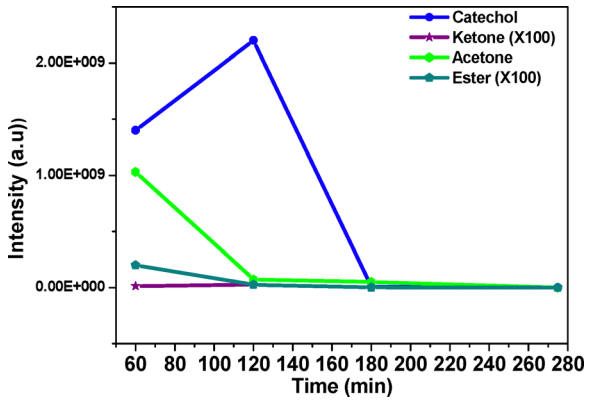

Fig. 14 Variation of the intensities in the mass spectra of the major intermediates as a function of time for the CN photocatalyst.

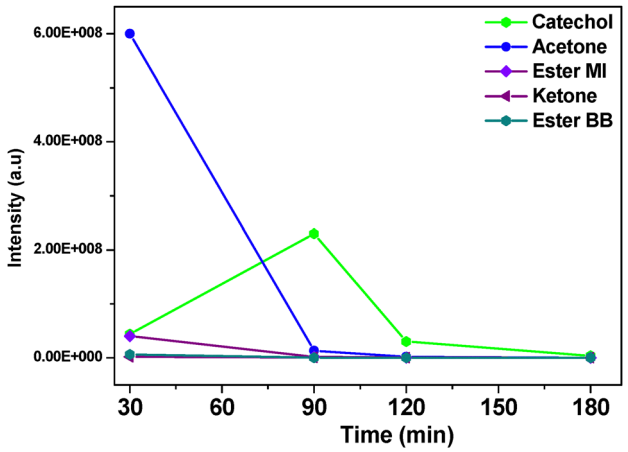

Fig. 15 Variation of the intensities in the mass spectra of the major intermediates as a function of time for the BSN–CN photocatalyst.

Mass spectra peaks are observed at *m*/*z* values of 116, 131 and 145. The peak at *m*/*z* of 145 represents the butyl butyrate ester formed mainly by opening of the ring. The ester may be formed from butanoic acid formed from the butanal and butanol. The peak at *m*/*z* 131 is mainly due to a benzyl ketonic intermediate of $C_7H_4O_2^-$,[58] which is probably the one from which the ring opening occurs. The peak at *m*/*z* of 116 with smaller fragments at 115 and 114 represents mainly chlorobenzene mainly formed by losing one Cl from either *o*-DCB or chlorophenol. The intermediates as shown by the CN photocatalyst are quite different as compared to that of the BSN photocatalyst and are represented in Scheme 5.

D. BSN–CN. The different intermediates formed by the BSN–CN photocatalyst are depicted in Fig. 12D as a function of degradation time. The different products formed are a mixture of both BSN and the CN catalysts together. After 60 min of irradiation, the different mass peaks that were obtained are at *m*/*z* values of 63, 76, 88, 89, 106, 105, 112, 116, 131, 145, 158 and 160. As understood above, the peak at *m*/*z* of 64 mostly represents a dimer of Cl^{35} or acetone; the peak at *m*/*z* 74 and with fragments at 88 and 89 represents an ester of CH_3–O–COO–C_2H_4 known as a McLafferty ion. The peaks with *m*/*z* of 105, 106 and 112 represent catechol; the peak at *m*/*z* of 116 with smaller fragments at 115 and 114 represents mainly chlorobenzene; the peak at *m*/*z* 131 is mainly due to a benzyl ketonic intermediate of $C_7H_4O_2^-$; the peak at *m*/*z* of 145 represents the butyl butyrate ester formed mainly by opening of the ring. It is quite interesting that the mass peaks at 131 and 145 have stronger intensity with BSN–CN as compared to that with CN, implying that these intermediates are formed in greater concentrations over the heterojunction structure as compared to only CN. The kinetics for the formation of the different intermediates from *o*-DCB are represented in Fig. 15 and are shown in Scheme 6.

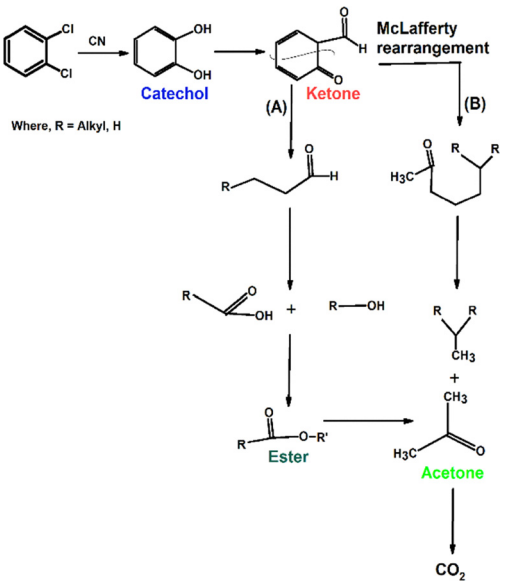

Scheme 5 Plausible intermediates formed by the CN photocatalyst from the ESI-MS data.

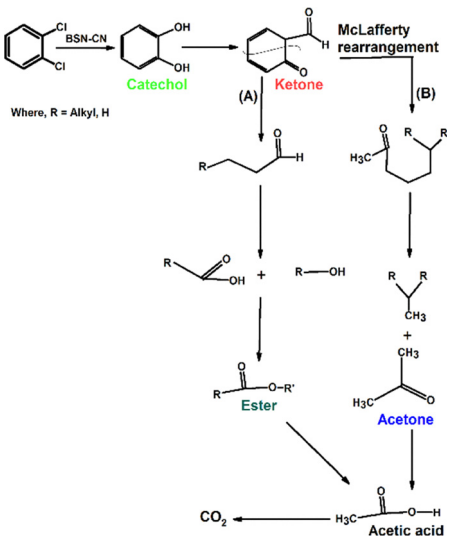

Scheme 6 Plausible intermediates formed by the BSN–CN photocatalyst from the ESI-MS data in both (A) and (B) pathways.

3.13. Post-XPS

XPS measurements of the catalysts after the photocatalytic reaction are shown in Fig. 16. The Bi-4f peaks are obtained at binding energies of 158.6 and 164 eV for Bi $4f_{7/2}$ and Bi $4f_{5/2}$, respectively, for the BSN–CN-15 sample, and similarly for the BSN sample the Bi $4f_{7/2}$ can be deconvoluted into two peaks at 159.1 and 157.5 eV binding energies along with a similar deconvolution of the Bi $4f_{5/2}$ peak at 164.4 and 162.84 eV binding energies. The XPS spectrum of the BSN before catalysis (Fig. 6C(b)) shows peaks at binding energies of 158.8 and 164.1 eV, respectively. This clearly shows that the intermediates formed like acetates (Scheme 2) *etc.* are formed over the Bi of the BSN surface and the Bi goes to a lower oxidation state.

However, in the BSN–CN heterojunction the Bi of the BSN does not form any lower oxidation state, though there is a small lowering in the binding energy by around 0.2 eV showing that the Bi has mostly oxidised the materials and the electron density is received from the Bi of the BSN–CN. Similarly, the Sn 3d for the BSN–CN (Fig. 16B) has peaks at binding energies (BE) of 490.9 and 499.3 for ($3d_{5/2}$ and $3d_{3/2}$) and BSN has the

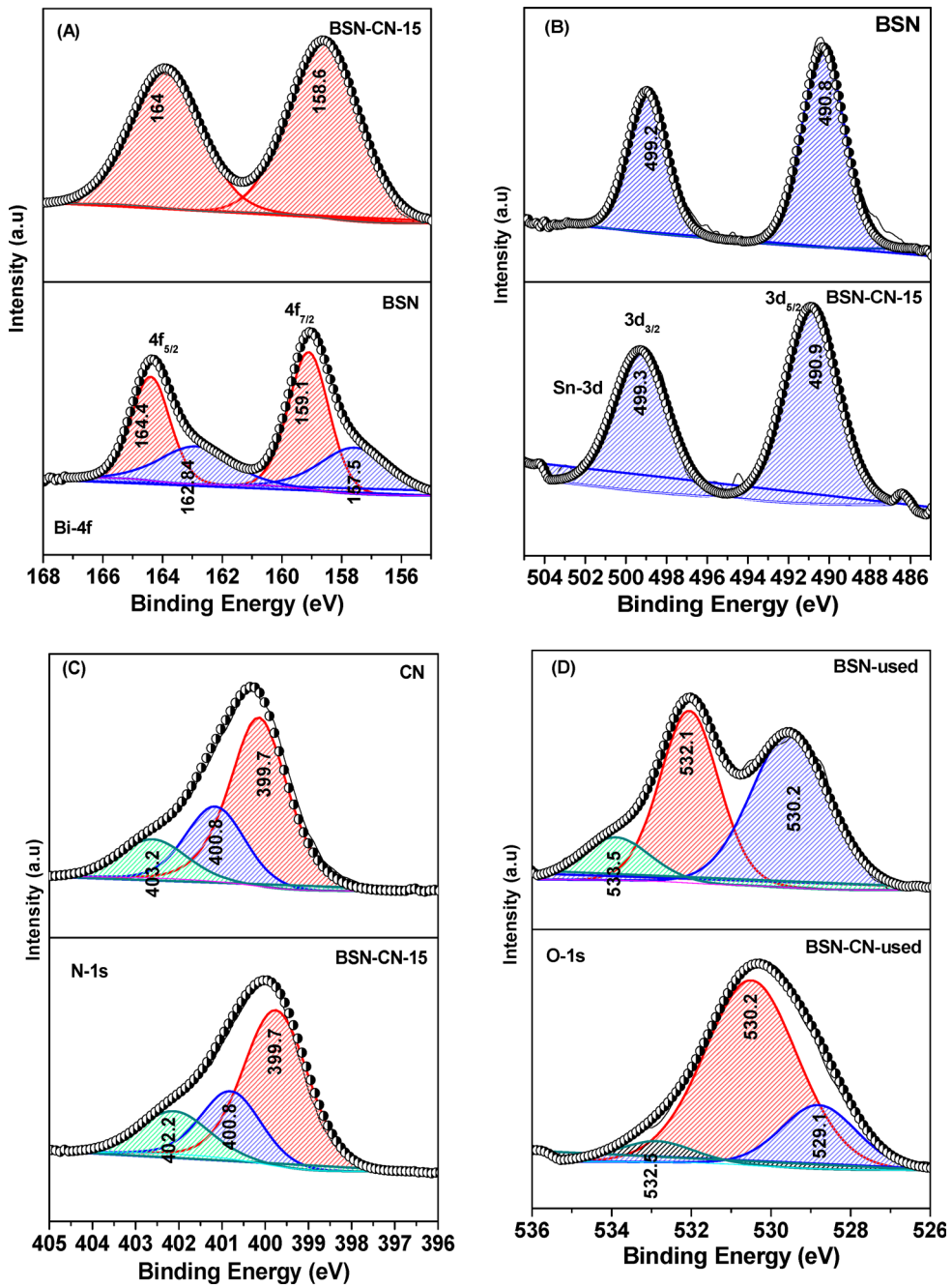

Fig. 16 XPS spectra of the photocatalysts after catalytic activity: (A) Bi-4f for BSN and BSN–CN-15; (B) Sn-3d for BSN and BSN–CN-15; (C) N-1s for CN and BSN–CN-15; and (D) O-1s for BSN and BSN–CN-15.

same at 490.8 and 499.2 eV, respectively. There is very little shift in the Sn-3d peaks for the catalysts (Fig. 6D), showing that the Sn remains electronically almost unaltered during the catalytic reactions.

The N-1s for the CN after reaction are present at BE of 399.7, 400.8 and 403.2 eV. In the main CN, the N-1s was represented by 3 main signals located at BE of 398.2 eV, 399.3 eV and 400.7 eV, corresponding to pyridinic N in a heptazine ring (C–N═C), pyrrolic nitrogen (from a triazole moiety) and the overlap of quaternary nitrogen, respectively. The evident increase in the BE of N-1s for CN mainly represents the withdrawal of electron density by the intermediates to stabilize over the CN surface and mainly the quaternary nitrogen to produce stable intermediates (as shown in Scheme 4) with N^+ of quaternary N. The O-1s peaks for the different BSN materials are found at BE of 530.2, 532.1, and 533.5 eV, and those for BSN–CN are obtained at BE of 529.1, 530.2 and 532.1 eV. Post-reaction, a shift of ~1.2 eV toward higher BE is observed for BSN (Fig. 16D), along with a clear decrease in the intensity of the O-vacancy peak (~533.5eV). For BSN–CN, the increase in the BE is lower compared to BSN, and is ~0.4. This also shows that there is a definite interaction between the O of the BSN and the BSN–CN and the intermediates. The stronger interaction of BSN shows stronger nucleophilic sites and weaker ones in the case of BSN–CN.

4. Discussion

Cyclic voltammetry (CV) results (Fig. 8A) clearly show a distinct cyclic voltammogram for BSN–CN-15 when compared to those of individual CN and BSN, providing initial evidence of heterojunction formation. Further support for the successful formation of this heterojunction comes from the elemental mapping of the FE-SEM data set for BSN–CN-15, which unambiguously confirms the co-localization of Bi, Sn, O, C, and N. We evaluated the photocatalytic activity for *o*-DCB degradation using CN, BSN, and various BSN–CN heterojunctions. Our findings indicate a direct correlation between increased BSN content in the BSN–CN heterojunction system and enhanced photocatalytic performance (Fig. 10A). This is best summarized by the observed activity trend: BSN–CN-15 > BSN–CN-10 > BSN–CN-5 > BSN–CN-1 > BSN > CN. The different intermediates formed during this process were largely identified through *ex situ* ESI-MS analysis. Several factors contribute to the superior photocatalytic activity of these heterojunctions, including:

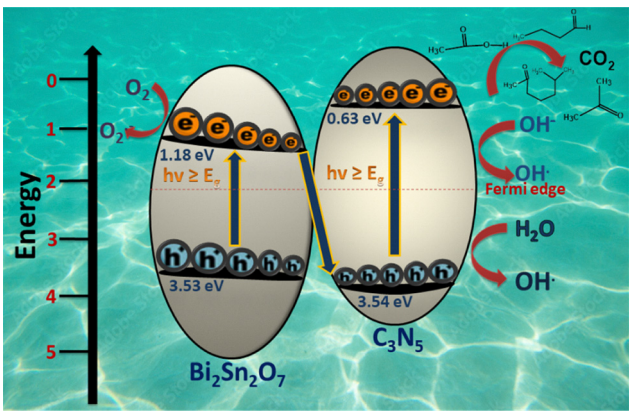

Scheme 7 S-scheme for the BSN–CN heterojunction and effective photocatalytic activity for the materials along with intermediates.

(i) S-scheme heterojunction

The efficacy of a heterojunction is controlled by different factors like (a) contact between the primary components; (b) formation of an inbuilt electric field at the interface; (c) the positions of the CB and VB play a critical role; (d) built-in electric field and potential barriers at the heterojunction interface also depend on other factors such as semi conductivity (n-type or p-type); (e) the work function; (f) Fermi level. Formation of a g-C_3N_5-pyrochlore heterojunction is an example of a van der Waals heterojunction,[75] where the two or more different materials are mainly held together by van der Waals forces, and this enhances the photocatalytic performance of the individual components. Usually the van der Waals heterojunction possesses a familiar Z scheme type of charge separation mechanism and certain of them may possess a S-scheme for the charge separation. The "S-scheme" refers to a small band of photocatalysts in which an oxidation photocatalyst (mainly like BSN) is coupled with a reduction photocatalyst (mainly g-C_3N_5). The oxidation photocatalyst has a higher oxidation potential, and the reduction photocatalyst has a higher reduction potential. The electron transfer in the S-scheme is like a 'step' from the macroscopic viewpoint and resembles the letter 'N' from the microscopic viewpoint. The importance of the S-scheme lies in the fact that it possesses (a) enhanced charge separation; (b) preserved redox ability. Type-II heterojunctions, while also separating charges, can suffer from reduced redox ability due to the repulsion between photogenerated electrons and holes at the interface. S-schemes overcome this limitation by directly transferring electrons to the valence band of the other semiconductor with a thermodynamically stable redox couple. This will facilitate the direct transfer of electrons by the S-scheme favouring the formation of the superoxide radical, which is effectively formed by the BSN–CN heterojunction, as evidenced in Fig. 5A(c). Another generic way to show the S-scheme is by XPS: if the binding energies of one semiconductor shift positively while those of the other shift negatively, it indicates electron transfer from the former to the latter, confirming the S-scheme mechanism. Though not an *in situ* XPS experiment here (where the catalyst is exposed to light whilst measuring the XPS), once we take a closer look at the XPS data set for the BSN–CN and BSN and CN separately, it is quite evident that (I) there is a depletion of the electron density around Bi due to the formation of the BSN–CN composite. The Bi-4f (Fig. 6C) in the present manuscript shows two prominent peaks, after l-s coupling, corresponding to binding energies of 158.8 eV (Bi $4f_{7/2}$) and 164.1 eV (Bi $4f_{7/2}$) for the BSN catalyst, which is in accordance with the previous literature. However, for the different composite materials, there is a slight shift in the binding energy towards the higher BE. The Bi $4f_{7/2}$ of

BSN–CN-1 has BE of 159 eV and that of the BSN–CN-15 has 159.1 eV. (II) Upon formation of the BSN–CN composite, there is an increase in the electron density around both C and N for the CN, as reflected in the XPS data of C-1s and N-1s for these samples (Fig. 6A and B), respectively. Therefore, the spin-trapping experiment using EPR, along with the charge separation evidenced by the XPS study, clearly shows the formation of an S-scheme heterojunction, as shown in Scheme 7.

(ii) Surface charge

As a heterogeneous catalytic reaction involving both solid and liquid phases, the surface charge of our photocatalysts plays a crucial role in the adsorption of reactants and intermediates. Previous studies by Adarsh *et al.*[18,76] have shown that *o*-DCB is typically adsorbed as highly nucleophilic enolates and phenolates. Our findings reveal that BSN exhibits a positive surface charge, while CN has a negative surface charge (Fig. 9B(b)). Interestingly, as the BSN content in the BSN–CN heterojunction increases, the surface charge behavior shifts. For BSN–CN-1 and BSN–CN-5, the surface charge is initially lower compared to pure CN. However, with higher percentages of BSN, such as in BSN–CN-10 and BSN–CN-15, the surface charge becomes predominantly positive, reflecting the dominant influence of BSN in the heterojunction. This positive surface charge on the BSN-rich composites is expected to stabilize the negatively charged enolate and phenolate intermediates, thereby leading to a faster reaction rate.

(iii) Band gap

The band gap of the BSN–CN heterojunction plays a critical role in its photocatalytic efficiency. It is observed that the band gap consistently decreases with more BSN, mostly due to the strain, particle size and effect of the incremental space charge as a function of the BSN concentration in the BSN–CN heterojunction photocatalyst. This reduction in the band gap is directly linked to the enhanced absorption of visible-light irradiation and significantly influences the kinetics of the photocatalytic reaction. Consequently, the progressive lowering of the band gap with increasing BSN content in the heterojunction directly correlates with the observed improvement in the photocatalytic properties, as evidenced by the enhanced mineralization of *o*-DCB by these catalysts.

(iv) VB potential

While the valence band (VB) oxidation potential of BSN is inherently higher than that of CN, we observed a decrease in the VB oxidation potential as BSN was dispersed within the BSN–CN heterojunction. The lowering of the VB potential is mostly due to the effect of the higher Schottky barrier formed in the BSN–CN heterojunction. Despite this reduction in the VB oxidation potential, it should be understood that although the valence band potential decreases, the electron transfer occurs directly through the S-scheme, thereby enhancing the photo-oxidation kinetics. The higher space charge also results in the direct transfer of the e-over this higher VB potential acting as deep electron traps, thereby increasing the lifetime of the h^+ usually used for the oxidation reaction. The effective VB potential for these heterojunctions remains sufficiently high to effectively mineralize *o*-DCB and its various intermediates as has been observed (Scheme 4–6).

(v) PL emission and TRPL understanding

Photoluminescence (PL) emission data (Fig. 10A) reveal a significant finding: photoluminescence (PL) and time-resolved photoluminescence (TRPL) data provide compelling evidence for how the addition of BSN enhances the photocatalytic activity of the BSN–CN heterojunction. A key finding from PL emission data is the reduction in PL intensity as the BSN concentration increases, which directly points to a decrease in the electron–hole recombination rate. This indicates that BSN effectively separates charge carriers, allowing them to participate in reactions rather than simply recombining and releasing energy as light. This is further supported by TRPL analysis, which shows a significant extension of the average electron–hole pair lifetime. For example, the lifetime increases from approximately 5.56 ns for pure CN to 6.35 ns for BSN–CN-15, demonstrating that charge carriers in the BSN–CN composite have a longer lifespan. The hydrothermal synthesis method used to create this material is crucial because it generates beneficial interfacial defect states that act as shallow traps, promoting charge transfer across the BSN–CN junction. These are not the uncontrolled bulk defects that would typically lead to non-radiative recombination and reduced activity. The analysis of our TRPL fits confirms this balance; the absence of a "peak-then-decline" behavior in carrier lifetime indicates that the defect density never reaches a detrimental, recombination-dominated state within our tested compositional range. Instead, these interfacial defects work in harmony with the favourable band alignment between BSN and CN, efficiently extracting carriers before deep-trap recombination can occur. This synergistic effect explains why we see a continuous, monotonic improvement in both carrier lifetime and photocatalytic performance up to 15 wt% BSN (Table 4), without an optimal concentration being reached. Ultimately, the TRPL data confirms BSN–CN-15 as the best photocatalyst in our series, proving that the introduced defects do not hinder the degradation of *o*-DCB.

(vi) Photocurrent

The higher photocurrent observed for BSN–CN (Fig. 9B) compared to individual CN and BSN indicates a significantly enhanced hole (h^+) current within the heterojunction. This increased charge separation and transfer efficiency directly contribute to the superior photocatalytic activity. Furthermore, this enhanced photocurrent also serves as evidence of the reusability of these materials as photocatalysts.

(vii) Intermediates

The distinct chemical compositions of CN and BSN lead to the formation of different sets of intermediates during *o*-DCB degradation. The lone pair electrons on the nitrogen centres of the conjugated CN structure provide basic sites that significantly influence intermediate formation. Similarly, the lone pair electrons on the Bi-1s orbital in BSN also plays a crucial

role. Both these factors, along with the varying surface charges, dictate the specific intermediates observed on each surface. Specifically, the intermediates formed over CN (Scheme 3) predominantly include electron-rich ketonic species. This is primarily due to the readily accessible electron density on the nitrogen centres of CN, a feature missing from the BSN surface. This electron density facilitates processes like McLafferty rearrangement, leading to a different array of intermediates.

Interestingly, the BSN–CN heterojunctions exhibit a combined intermediate formation pathway, reflecting the contributions of both CN and BSN surfaces. Kinetic studies of intermediate degradation (Fig. 13–15) revealed the prevalent formation of catechol. This is consistent with *o*-DCB's typical adsorption as catecholate or phenolate in aqueous environments, leading to these initial intermediates. Significantly, both catechol and acetone are degraded at a much faster rate, exhibiting mostly second-order kinetics (Fig. 15). This efficient degradation of intermediates, leading to products, underscores their superior photocatalytic performance compared to BSN or CN alone, as depicted in Scheme 7.

Post-reaction XPS data provides further insight into the mechanism. It is quite clear from the post-XPS studies that surface sites over which the reactants and intermediates are formed and adsorbed are mainly Bi, N and O of the heterojunction. Therefore, post-catalysis, most of the reactive sites will be occupied by the reactants or the intermediates, leading to a decrease in the catalytic efficiency. As can be observed from Table S5 and Table S6, showing the elemental analysis of the elements from the XPS study for the photocatalysts after the catalytic reaction, it is quite clear that there is no leaching from the surface, which is unusual for the catalytic reaction. The g-C_3N_5 and $Bi_2Sn_2O_7$ and even the heterojunctions of BSN–CN are photo-stable materials, as has been understood from the long photo-switching experiments, as has been described in this manuscript, as shown in Fig. 9B. Therefore, mostly the lowering in the catalytic efficiency was due to the lowering of the active sites over the catalytic surface by either the intermediates or the adsorbed reactants. This demonstrates the strong utilization of oxygen vacancies in the BSN–CN materials compared to BSN. The detection of a lower oxidation state of Bi in BSN after the reaction suggests the formation of surface intermediates over the Bi sites and the involvement of the Bi-lone pair electrons in their formation. For CN, the quaternary nitrogen (N^+) centres are primarily responsible for stabilizing these intermediates. However, in the heterojunctions, while Bi shows a small decrease in electron density, the N^+ of quaternary nitrogen exhibits a more significant increase in binding energy, indicating that the intermediates are predominantly stabilized by the CN component.

5. Conclusion

A novel heterojunction has been successfully hydrothermally synthesized and used as a photocatalyst by integrating various amounts of BSN with CN, both materials possessing remarkably similar band gaps. These materials proved highly effective in the mineralization of *o*-DCB, achieving complete degradation within 180–290 minutes, demonstrating their potential as efficient photocatalysts. Through detailed *ex situ* ESI-MS analysis, various intermediates were identified during the degradation of *o*-DCB, and a comprehensive photocatalytic reaction mechanism was established. The lowering of the band gap as a function of BSN in the BSN–CN heterojunction can be understood on the basis of the particle size effect, strain formed by the presence of the BSN in BSN–CN and space charge formed by the heterojunction of the BSN–CN. The change in the valence band potential could also be explained in terms of upward bending resulting from the formation of the BSN–CN heterojunction Schottky barrier. The enhanced photocatalytic activity of these heterojunctions is attributed to key factors including their surface charge, optimized band gap, favourable valence band potential and space charge formed due to the formation of the heterojunction, including the nature of the intermediates formed. Our comparative studies clearly show a distinct trend in photocatalytic activity: BSN–CN-15 > BSN–CN-10 > BSN–CN-5 > BSN–CN-1 > BSN > CN, with BSN–CN-15 exhibiting superior performance. The effective increase in the kinetics of the BSN–CN is primarily due to the S-scheme transfer of the e^- and h^+. Individual BSN primarily yields catechol, esters, and acetone, whereas CN produces catechol, ketones, esters, and acetone. The BSN–CN heterojunctions, however, produce a mixture of both. Crucially, the formation of these heterojunctions significantly extends the lifetime of holes, and this effect increases proportionally with the amount of BSN incorporated, contributing to their superior photocatalytic efficiency.

Author contributions

AK has performed the synthesis, carried out the characterisations and completed the photocatalytic reaction including the intermediate study in the ESI-MS and prepared the first draft of the manuscript. DT has done the XPS experiments for the BSN–CN samples and the used samples. SM has contributed to the Mött–Schottky experiments, spin-trapping and control experiments and strain calculations. FE-SEM, elemental mapping and the EDS results were taken by JB. AKT was consulted in every step for scientific input and has checked the manuscript and has helped immensely in understanding of the data. KB has conceptualised the problem, written the manuscript, analysed all datasets and guided AK and SM in every step of this manuscript.

Conflicts of interest

The authors report no conflict of interest.

Data availability

Data will be available upon request from the authors.

Supplementary information (SI): this supplementary data includes a comprehensive set of figures and tables. Fig. S1–S7 present UV-Vis data detailing the degradation of *o*-DCB under

visible-light irradiation, investigating its self-degradation, adsorption and degradation using various catalysts: BSN, CN, and BSN–CN composites at different dispersion percentages (1, 5, 10, and 15). Fig. S8 shows the CV of g-C_3N_5 with different scan rates; Fig. S9 illustrates the photocatalytic reactor used for the experiments. Fig. S10 showcases the mass spectrometry (MS) data for the oxidation products of *o*-DCB using BSN, CN, BSN–CN-1, and BSN–CN-15 catalysts in a closed photocatalytic reactor under visible light; Fig. S11 provides the mass spectra of atmospheric air. Fig. S12 shows the long-time XRD (1 h) of the BSN–CN-15 as a function of temperature: (a) 350 °C; (b) 500 °C; and (c) 750 °C. Fig. S13 shows the Rietveld refinement plot for BSN–CN-15-750 °C. Fig. S14 shows the Williamson–Hall plot to determine the strain calculation (in eqn (S13)). Fig. S15 shows the SEM images for the used BSN–CN-15 samples with elemental mapping for the different elements: (a) Bi-Mα; (b) C-Kα; (c) N-Kα; (d) O-Kα; and (e) Sn-Lα; and (f) EDS spectra for the sample. Scheme S1: C1c1 monoclinic $Bi_2Sn_2O_7$ with lattice parameters of a = 13.15; b = 7.54; c = 16.01; $\alpha = \beta = 90°$; γ = 125.012° – ICSD-239965. Table S1 EDS data for the BSN–CN-15 photocatalyst. Table S2 apparent quantum efficiencies for the different photocatalysts. Table S3 SAED pattern calculation for Fig. 2A (BSN–CN-15) showing the different planes as compared to ICSD-File-239965. Table S4 SAED pattern calculation for Fig. 2B (BSN–CN-15) showing the different planes as compared to ICSD-File-239965. Table S5 elemental analysis from XPS of the BSN sample before and after catalysis. Table S6 elemental analysis from XPS of the BSN–CN-15 sample before and after catalysis. Table S7 elemental analysis from the EDS analysis of the (a) BSN–CN-15 after catalysis from Fig. S15f and b BSN–CN-15-sample before catalysis Fig. 3C. See DOI: **https://doi.org/10.1039/d5ma00954e**.

Acknowledgements

We acknowledge Shri. Sai Rekapalli of TIFR for helping in the *ex situ* ESI-MS experiment. Dr V. Viswanadh of MSD, BARC for taking the HR-TEM and TEM images and Dr G. Mane, Sunandan Divatia School of Science, NMIMS (Deemed to be University) for helping us in the synthesis of CN and Ms Reshmi T. P. RCD, BARC for helping in the TRPL experiments. Mr Santosh Sahu and Mr S. Narang from Chemistry Division, BARC are acknowledged for XRD and discussion in Rietveld refinement. Komal Thawrani of TIFR is acknowledged for helping us in the EPR spin-trapping experiments.

References

1 K. Bhattacharyya, J. Majeed, K. K. Dey, P. Ayyub, A. K. Tyagi and S. R. Bharadwaj, *J. Phys. Chem. C*, 2014, **118**, 15946–15962, DOI: **10.1021/jp5054666**.
2 K. Bhattacharyya, G. P. Mane, V. Rane, A. K. Tripathi and A. K. Tyagi, *J. Phys. Chem. C*, 2021, **125**, 1793–1810, DOI: **10.1021/acs.jpcc.0c08441**.
3 R. G. Nair, S. Mazumdar, B. Modak, R. Bapat, P. Ayyub and K. Bhattacharyya, *J. Photochem. Photobiol., A*, 2017, **345**, 36–53, DOI: **10.1016/j.jphotochem.2017.05.016**.
4 P. Mandal, A. Kumar, J. Bahadur, M. D. Mukadam, D. Sen and K. Bhattacharyya, *ACS Appl. Nano Mater.*, 2024, **7**, 17533–17552, DOI: **10.1021/acsanm.4c02663**.
5 K. Bhattacharyya, S. Varma, A. K. Tripathi, A. Vinu and A. K. Tyagi, *Chem. - Eur. J.*, 2011, **17**, 12310–12325, DOI: **10.1002/chem.201001121**.
6 J. Ran, B. Zhu and S. Z. Qiao, *Angew. Chem., Int. Ed.*, 2017, **56**, 10373–10377, DOI: **10.1002/anie.201703827**.
7 S. Qin, L. Huang, Y. Zhang, T. Zhang, M. Tian and J. Jiang, *Sci. Rep.*, 2025, **15**, 787, DOI: **10.1038/s41598-025-85268-9**.
8 J. Wu, F. Huang, X. Lü, P. Chen, D. Wan and F. Xu, *J. Mater. Chem.*, 2011, **21**, 3872–3876, DOI: **10.1039/C0JM03252B**.
9 D. Li and J. Xue, *New J. Chem.*, 2015, **39**, 5833–5840, DOI: **10.1039/C5NJ00886G**.
10 J. Wen, J. Xie, X. Chen and X. Li, *Appl. Surf. Sci.*, 2017, **391**, 72–123, DOI: **10.1016/j.apsusc.2016.07.030**.
11 G. P. Mane, S. N. Talapaneni, K. S. Lakhi, H. Ilbeygi, U. Ravon, K. Al-Bahily, T. Mori, D. H. Park and A. Vinu, *Angew. Chem., Int. Ed.*, 2017, **56**, 8481–8485, DOI: **10.1002/anie.201702386**.
12 I. Y. Kim, S. Kim, X. Jin, S. Premkumar, G. Chandra, N. S. Lee, G. P. Mane, S. J. Hwang, S. Umapathy and A. Vinu, *Angew. Chem.*, 2018, **130**, 17381–17386, DOI: **10.1002/ange.201811061**.
13 P. Kumar, E. Vahidzadeh, U. K. Thakur, P. Kar, K. M. Alam, A. Goswami, N. Mahdi, K. Cui, G. M. Bernard and V. K. Michaelis, *J. Am. Chem. Soc.*, 2019, **141**, 5415–5436, DOI: **10.1021/jacs.9b00144**.
14 M. Li, Q. Lu, M. Liu, P. Yin, C. Wu, H. Li, Y. Zhang and S. Yao, *ACS Appl. Mater. Interfaces*, 2020, **12**, 38266–38274, DOI: **10.1021/acsami.0c11894**.
15 B. Debnath, S. Singh, S. M. Hossain, S. Krishnamurthy, V. Polshettiwar and S. Ogale, *Langmuir*, 2022, **38**, 3139–3148, DOI: **10.1021/acs.langmuir.1c03127**.
16 Y. Wang, T. N. Pham, Y. Tian, Y. Morikawa and L. Yan, *J. Colloid Interface Sci.*, 2021, **585**, 740–749, DOI: **10.1016/j.jcis.2020.10.054**.
17 A. Pal, T. K. Dey, K. Bhattacharyya and R. C. Bindal, *Mater. Adv.*, 2020, **1**, 403–414, DOI: **10.1039/D0MA00107D**.
18 K. Bhattacharyya, A. Kumar, D. Tyagi, A. K. Tripathi and A. K. Tyagi, *ChemPhysChem*, 2024, **25**, e202300472, DOI: **10.1002/cphc.202300472**.
19 E. Elhaddad, W. Rehman, M. Waseem, M. Nawaz, S. Haq and C.-Y. Guo, *J. Inorg. Organomet. Polym. Mater.*, 2021, **31**, 172–179, DOI: **10.1007/s10904-020-01726-z**.
20 F. Huang, G. Li, T. Fan, W. Wang, K. An and J. Wang, *Appl. Surf. Sci.*, 2024, **643**, 158674, DOI: **10.1016/j.apsusc.2023.158674**.
21 J. Zhang, G. Yu, C. Yang, W. Zhao, Z. Duan, H. Liu and S. Li, *SusMat*, 2025, **5**, e70002, DOI: **10.1002/sus2.70002**.
22 S. Li, X. Li, Y. Liu, P. Zhang, J. Zhang and B. Zhang, *Chin. J. Catal.*, 2025, **72**, 130–142, DOI: **10.1016/S1872-2067(25)64652-3**.
23 D. Ma, Q. Xue, Y. Liu, F. Liang, W. Li, T. Liu, C. Zhuang, Z. Zhao and S. Li, *J. Mater. Sci. Technol.*, 2025, **243**, 265–274, DOI: **10.1016/j.jmst.2025.05.011**.

24 S. Li, C. You, K. Rong, C. Zhuang, X. Chen and B. Zhang, *Adv. Powder Mater.*, 2024, **3**, 100183, DOI: 10.1016/j.apmate.2024.100183.
25 V. Jayaraman and A. Mani, *Sep. Purif. Technol.*, 2020, **235**, 116242, DOI: 10.1016/j.seppur.2019.116242.
26 K. Annamalai, N. R. Sasirekha and S. Balakumar, *Surf. Interfaces*, 2024, **53**, 105071, DOI: 10.1016/j.surfin.2024.105071.
27 X. Yin, X. Li, W. Gu, F. Wang, Y. Zou, S. Sun, Z. Fu and Y. Lu, *ACS Appl. Mater. Interfaces*, 2017, **9**, 19908–19916, DOI: 10.1021/acsami.7b04587.
28 A. Kumar, D. Tyagi, R. Kumar, M. Ghosh, B. P. Mandal, A. Roy, S. Nath, A. K. Tyagi and K. Bhattacharyya, *J. Mater. Chem. A*, 2025, **13**, 19795–19820, DOI: 10.1039/D5TA01746G.
29 B. Liu, X. Li, Q. Zhao, J. Ke, M. Tadé and S. Liu, *Appl. Catal., B*, 2016, **185**, 1–10, DOI: 10.1016/j.apcatb.2015.12.003.
30 X. Zou, Y. Dong, X. Zhang, Y. Cui, X. Ou and X. Qi, *Appl. Surf. Sci.*, 2017, **391**, 525–534, DOI: 10.1016/j.apsusc.2016.06.003.
31 X. Zou, Y. Dong, S. Li, J. Ke, Y. Cui and X. Ou, *J. Taiwan Inst. Chem. Eng.*, 2018, **93**, 158–165, DOI: 10.1016/j.jtice.2018.05.041.
32 J. Sun, X. Li, Q. Zhao, M. O. Tadé and S. Liu, *Appl. Catal., B*, 2017, **219**, 259–268, DOI: 10.1016/j.apcatb.2017.07.052.
33 F. Zhang, X. Li, Q. Zhao and A. Chen, *J. Phys. Chem. C*, 2016, **120**, 19113–19123, DOI: 10.1021/acs.jpcc.6b03618.
34 F. Zhang, X. Li, Q. Zhao, G. Chen and Q. Zhang, *Appl. Catal., B*, 2020, **263**, 118278, DOI: 10.1016/j.apcatb.2019.118278.
35 R. D. Shannon, J. D. Bierlein, J. L. Gillson, G. A. Jones and A. W. Sleight, *J. Phys. Chem. Solids*, 1980, **41**, 117–122, DOI: 10.1016/0022-3697(80)90041-4.
36 T. T. Zhang, K. W. Li, J. Zeng, Y. L. Wang, X. M. Song and H. Wang, *J. Phys. Chem. Solids*, 2008, **69**, 2845–2851, DOI: 10.1016/j.jpcs.2008.07.014.
37 F. Fina, S. K. Callear, G. M. Carins and J. T. S. Irvine, *Chem. Mater.*, 2015, **27**, 2612–2618, DOI: 10.1021/acs.chemmater.5b00411.
38 B. V. Lotsch, M. Döblinger, J. Sehnert, L. Seyfarth, J. Senker, O. Oeckler and W. Schnick, *Chem. - Eur. J.*, 2007, **13**, 4969–4980, DOI: 10.1002/chem.200601759.
39 S. Rana, A. Kumar, T. Wang, P. Dhiman, G. Sharma and H. Shi, *Chemistry*, 2024, **6**, 962–980, DOI: 10.3390/chemistry6050056.
40 S. Heidari, M. Haghighi and M. Shabani, *Chem. Eng. J.*, 2020, **389**, 123418, DOI: 10.1016/j.cej.2019.123418.
41 A. Uihlein, L. Pflug and M. Stingl, *PAMM*, 2023, **22**, e202200047, DOI: 10.1002/pamm.202200047.
42 A. Walsh, G. W. Watson, D. J. Payne, G. Atkinson and R. G. Egdell, *J. Mater. Chem.*, 2006, **16**, 3452–3458, DOI: 10.1039/B606413B.
43 H. T. Vuong, D. V. Nguyen, L. P. Phuong, P. P. D. Minh, B. N. Ho and H. A. Nguyen, *Carbon Neutralization*, 2023, **2**, 425–457, DOI: 10.1002/cnl2.65.
44 K. Thawrani, K. Bhattacharya, D. Khushalani and J. Dasgupta, *J. Mater. Chem. A*, 2025, **13**, 28934–28943, DOI: 10.1039/D5TA02777B.
45 C. You, C. Wang, M. Cai, Y. Liu, B. Zhu and S. Li, *Acta Phys.-Chim. Sin.*, 2024, **40**, 2407014, DOI: 10.3866/PKU.WHXB202407014.
46 R. Nautiyal, S. K. Gupta, M. Ghosh, C. A. Betty, N. Panangattu Dharmarajan, V. Narayanan, K. Bhattacharyya, A. Vinu and G. P. Mane, *Small Struct.*, 2025, 2400653, DOI: 10.1002/sstr.202400653.
47 Z. Zhao, F. Liu, L. Zhao and S. Yan, *Mater. Chem. Phys.*, 2010, **124**, 55–59, DOI: 10.1016/j.matchemphys.2010.07.062.
48 C. He, S. Sankarasubramanian, A. Ells, J. Parrondo, C. Gumeci, M. Kodali, I. Matanovic, A. K. Yadav, K. Bhattacharyya and N. Dale, *ACS Catal.*, 2021, **11**, 7006–7017, DOI: 10.1021/acscatal.1c00963.
49 M. Jafar, A. Kumar, V. G. Gupta, A. K. Tyagi and K. Bhattacharyya, *ACS Omega*, 2025, **10**, 13080–13104, DOI: 10.1021/acsomega.4c10501.
50 X. Liang, G. Wang, X. Dong, G. Wang, H. Ma and X. Zhang, *ACS Appl. Nano Mater.*, 2018, **2**, 517–524, DOI: 10.1021/acsanm.8b02089.
51 V. W.-h Lau, I. Moudrakovski, T. Botari, S. Weinberger, M. B. Mesch, V. Duppel, J. Senker, V. Blum and B. V. Lotsch, *Nat. Commun.*, 2016, **7**, 12165, DOI: 10.1038/ncomms12165.
52 Y. Cui, Z. Ding, X. Fu and X. Wang, *Angew. Chem., Int. Ed.*, 2012, **51**, 11814–11818, DOI: 10.1002/anie.201206534.
53 D. Li, L. Zeng, X. Li, X. Wang, H. Ma, S. Assabumrungrat and J. Gong, *Appl. Catal., B*, 2015, **176**, 532–541, DOI: 10.1016/j.apcatb.2015.04.020.
54 J. Fu, B. Chang, Y. Tian, F. Xi and X. Dong, *J. Mater. Chem. A*, 2013, **1**, 3083–3090, DOI: 10.1039/C2TA00672C.
55 C. Chang, L. Zhu, S. Wang, X. Chu and L. Yue, *ACS Appl. Mater. Interfaces*, 2014, **6**, 5083–5093, DOI: 10.1021/am5002597.
56 J. Yu, S. Wang, B. Cheng, Z. Lin and F. Huang, *Catal. Sci. Technol.*, 2013, **3**, 1782–1789, DOI: 10.1039/C3CY20878H.
57 P. Pascuta and E. Culea, *Mater. Lett.*, 2008, **62**, 4127–4129, DOI: 10.1016/j.matlet.2008.06.015.
58 S. Vadivel, P. Sujita, B. Paul, B. Vidhya, A. Sebastian and R. Selvarajan, *Catal. Commun.*, 2024, **187**, 106882, DOI: 10.1016/j.catcom.2024.106882.
59 X. Wang, *Modeling Semi-arid Water–Soil–Vegetation Systems in a Changing Climate*, IOP Publishing, 2022.
60 Z. Lu and Z. Tian, *Mater. Today Commun.*, 2023, **36**, 106474, DOI: 10.1016/j.mtcomm.2023.106474.
61 P. Yu, S. Chen, Y. Wang, J. Li, Z. Zhang, S. Zhao, Y. Zhang and Y. Zhou, *Int. J. Hydrogen Energy*, 2024, **58**, 1266–1276, DOI: 10.1016/j.ijhydene.2024.01.272.
62 Q. Liu, X. Ji, J. Deng, H. Jiang, G. Li, Y. Ouyang, X. Li, C. Tang, X. Tan and X. Hu, *J. Environ. Chem. Eng.*, 2023, **11**, 110153, DOI: 10.1016/j.jece.2023.110153.
63 Q. Yang, X. H. Cai, Y. Pang and M. Wang, *Int. J. Quantum Chem.*, 2020, **120**, e26378, DOI: 10.1002/qua.26378.
64 C.-H. Hu, X.-H. Yin, D.-H. Wang, Y. Zhong, H.-Y. Zhou and G.-H. Rao, *Chin. Phys. B*, 2016, **25**, 067801, DOI: 10.1088/1674-1056/25/6/067801.
65 A. Mehtab, S. Banerjee, Y. Mao and T. Ahmad, *ACS Appl. Mater. Interfaces*, 2022, **14**, 44317–44329, DOI: 10.1021/acsami.2c11140.
66 S. K. Gupta, K. Sudarshan, P. S. Ghosh, K. Sanyal, A. P. Srivastava, A. Arya, P. K. Pujari and R. M. Kadam, *RSC Adv.*, 2016, **6**, 3792–3805, DOI: 10.1039/C5RA23876E.

67 B. Zhu, Q. Dong, J. Huang, M. Yang, X. Chen, C. Zhai, Q. Chen, B. Wang, H. Tao and L. Chen, *ACS Omega*, 2023, **8**, 13702–13714, DOI: **10.1021/acsomega.2c07899**.
68 P. Niu, G. Liu and H.-M. Cheng, *J. Phys. Chem. C*, 2012, **116**, 11013–11018, DOI: **10.1021/jp301026y**.
69 T. F. Yeh, C. Y. Teng, S. J. Chen and H. Teng, *Adv. Mater.*, 2014, **26**, 3297–3303, DOI: **10.1002/adma.201305299**.
70 J. Zhang, Z. Li, B. Liu, M. Chen, Y. Zhou and M. Zhu, *Appl. Catal., B*, 2023, **328**, 122522, DOI: **10.1016/j.apcatb.2023.122522**.
71 A. M. Sadanandan, M. Fawaz, N. P. Dharmarajan, M. Huš, G. Singh, C. I. Sathish, B. Likozar, Z. Li, A. M. Ruban and C.-H. Jeon, *Appl. Catal., B*, 2025, **362**, 124701, DOI: **10.1016/j.apcatb.2024.124701**.
72 M. Takayama, M. Hashimoto, K. Ohshimo, F. Misaizu, M. Ubukata and K. Nagatomo, *Phys. Chem. Chem. Phys.*, 2025, **27**, 261–269, DOI: **10.1039/D4CP03577A**.
73 M. A. Fahmey, M. A. Zayed and Y. H. Keshk, *Thermochim. Acta*, 2001, **366**, 183–188, DOI: **10.1016/S0040-6031(00)00724-3**.
74 S. Wu, H. Ma, P. Iya, S. David and L. Pasa-Tolic, *The Encyclopedia of Spectroscopy and Spectrometry*, 3rd edn, 2017.
75 A. Balapure, J. R. Dutta and R. Ganesan, *RSC Appl. Interfaces*, 2024, **1**, 43–69, DOI: **10.1039/D3LF00126A**.
76 A. Kumar, D. Tyagi, S. Varma, H. Chand, V. Krishnan, K. Bhattacharyya and A. K. Tyagi, *Mater. Adv.*, 2024, **5**, 1301–1331, DOI: **10.1039/D3MA00628J**.